Journal of Computational Physics 228 (2009) 5207–5236

Contents lists available at ScienceDirect

Journal of Computational Physics

journal homepage: www.elsevier.com/locate/jcp

A transformation-free HOC scheme for incompressible viscous flows past an impulsively started circular cylinder

Jiten C. Kalita, Rajendra K. Ray *

Department of Mathematics, Indian Institute of Technology Guwahati, Assam 781039, India

ARTICLE INFO

Article history:
Received 29 August 2008
Received in revised form 2 March 2009
Accepted 8 April 2009
Available online 22 April 2009

AMS subject classification:
65N06
65Z05
65Y99

Keywords:
Transient
HOC
Navier–Stokes
Circular cylinder
Von Kármán street
Nonuniform polar grids

ABSTRACT

In this paper, we present a higher order compact scheme for the unsteady two-dimensional (2D) Navier–Stokes equations on nonuniform polar grids specifically designed for the incompressible viscous flows past a circular cylinder. The scheme is second order accurate in time and at least third order accurate in space. The scheme very efficiently computes both unsteady and time-marching steady-state flow for a wide range of Reynolds numbers (*Re*) ranging from 10 to 9500 for the impulsively started cylinder. The robustness of the scheme is highlighted when it accurately captures the vortex shedding for moderate *Re* represented by the von Kármán street and the so called α and β-phenomena for higher *Re*. Comparisons are made with established numerical and experimental results and excellent agreement is found in all the cases, both qualitatively and quantitatively.

1. Introduction

The classical problem of the evolution of incompressible viscous flow induced by an impulsively started circular cylinder is one of the most widely studied problems in computational fluid dynamics. It has continued to generate tremendous interest amongst researchers over the last century mainly because of the fact that it displays almost all the fluid mechanical phenomena for incompressible viscous flows in the simplest of geometric settings. However, the flow structure is very complex, especially for large Reynolds numbers, thus making the computation of the flow even more challenging and intriguing. Because of its popularity, a plethora of experimental, theoretical and numerical results are readily available for this problem in the literature.

The theoretical studies related to this problem can be dated back to the work of Blasius [17] in 1908 which was generally based on the boundary layer theory. This was further persisted by Goldstein et al. [18], Schuh [19], Wundt [20] and Watson [21] all of whom considered the limiting case of infinite Reynolds number. Later on, Wang [22] and Collins and Dennis [23] extended this work for finite but higher Reynolds numbers. In all the cases, results could be found only for short span of time in the early stage of the flow after the start.

* Corresponding author. Tel.: +91 9435119120; fax: +91 3612582649.
E-mail addresses: jiten@iitg.ernet.in (J.C. Kalita), rkr@iitg.ernet.in (R.K. Ray).

0021-9991/$ - see front matter
doi:10.1016/j.jcp.2009.04.016

Besides these theoretical works, for a better understanding of the phenomena of the unsteady wake formation, several experimentalists [3,29–32,53–55] performed a series of tests based on the visualization the flow for various Reynolds numbers. These experimental works have been of immense help to the computational fluid dynamics community; new computational methods are being developed and consequently improved upon to solve this complex flow problem [24–26,28,33–44]. We now have enough experimental data that can be compared with the outcome of the numerical results, paving the way for computing complicated and extended flow phenomena for Reynolds numbers hitherto unexplored by experimentalists.

Over the years, the second order central difference schemes, because of their easy and straight-forwardness in application, have for quite some time been a popular choice for discrete approximation of partial differential equations. Such methods are known to yield quite good results on reasonable meshes if the solution is well behaved. But for certain problems, such as the convection dominated flows, the solution may exhibit oscillatory behaviour if the mesh is not sufficiently refined. However, mesh refinement invariably brings in additional points into the system resulting in an increased system size and consequently more memory and CPU time are required to solve such problems on a computer. Again discretization on a non-compact stencil (generally associated with higher-order accurate methods) increases the band-width of the coefficient matrix arising out of the discretization process. Both mesh refinement and increased matrix band-width ultimately result in increased arithmetic operations. Thus neither a lower-order accurate method on a fine mesh nor a higher-order accurate one on a non-compact stencil could be computationally cost-effective. Therefore, of late, the Higher Order Compact (HOC) finite difference schemes for the computation of incompressible viscous flows are gradually gaining popularity because of their high accuracy and advantages associated with compact difference stencils. A compact finite difference scheme is one which utilizes grid points located only directly adjacent to the node about which the differences are taken. In addition, if the scheme has an order of accuracy greater than two, it is termed a higher-order compact method. There exist several mechanisms through which finite difference schemes can achieve higher-order compactness. One of them is based on Padé [2] approximation, which is an implicit relation between the derivatives and functions at adjacent nodal points. These schemes [10,12–16] include information not only from the adjacent points to the node about which the differences are taken, but also includes information from nodal points located at distance two or three steps away from that node.

Another class of HOC schemes [4–9,11,45,47,49], which, in recent years have generated renewed interest amongst the computational fluid dynamics community are the ones which utilize grid points located only directly adjacent to the node about which the differences are taken and the dependent variable is explicitly present in the formulation unlike the one described in [10]. Most of these schemes were developed for equations of the convection–diffusion type and were well equipped to simulate incompressible viscous flows governed by the Navier–Stokes (N–S) equations as well. However majority of these HOC schemes developed so far are mostly on uniform grids [4,9,11,45,49]. The very few attempts that have been made to develop HOC scheme on nonuniform grids for the convection–diffusion equations [41,45–47] use the conventional transformation technique from the physical plane to the computational plane.

In a departure from this practice, Kalita et al. [5] developed an HOC scheme on rectangular nonuniform grids for the steady 2D convection–diffusion equation with variable coefficients without any transformation. It was based on the Taylor series expansion of a continuous function at a particular point for two different step lengths and approximation of the derivatives appearing in the 2D convection–diffusion equation on a nonuniform stencil. The original PDE was then used again to replace the derivative terms appearing in the finite difference approximations, resulting in a higher order scheme on a compact stencil of nine points.

In this paper, we extend the philosophy outlined in reference [5] to develop a transient HOC scheme for streamfunction-vorticity $(\psi - \omega)$ formulation of the 2D N–S equations on cylindrical polar coordinates. The basic difference between the proposed scheme and the earlier HOC schemes is that the present scheme is able to handle variable coefficients of the second order derivatives while the previous schemes could deal with unit diffusion coefficients only. This perhaps is the reason that majority of the earlier endeavors to develop HOC schemes on cylindrical polar coordinates were confined to the Poisson equation on uniform grids [48–52] only.

To validate the proposed scheme, we apply it to this well known problem of unsteady flow past an impulsively started circular cylinder for a wide range of *Re* ranging from 10 to 9500. In the process, we have also developed transient HOC approximation for the Neumann boundary condition for vorticity. For low and moderate *Re*, we compute the flow until steady-state or till the flow becomes periodic. For the higher range of *Re*, we compute the solution in the initial stages of the flow. For all the Reynolds numbers, detailed discussion on the flow structure and comparison with experimental and numerical results are provided. In each case, our solution agrees very well, both qualitatively and quantitatively with established numerical and experimental results, confirming the efficiency of the proposed scheme. The robustness of the scheme however is better realized when it captures the periodic nature of the flow for $Re = 60$ and 200 characterized by vortex shedding represented by the von Kármán street and also by the fact that it very accurately captures the so called secondary phenomena for moderate *Re*, and α and β-phenomena for higher *Re*.

The paper has been arranged in six sections. Section 2 deals with the problem and the governing equations, Section 3 with the mathematical formulation and discretization, Section 4 with the solution of the algebraic system of equations, Section 5 with the numerical results and discussion and finally, Section 6 summarizes the whole work.

2. The problem and the governing equations

We consider the unsteady, incompressible flow over an infinitely long cylinder of circular cross-section of radius R_0 (see the schematic diagram in Fig. 1). The flow is governed by the incompressible N–S equations. In non-dimensional form, the $\psi-\omega$ formulation of the N–S equations in cylindrical polar coordinates (r,θ) are given by,

$$\frac{\partial^2\omega}{\partial r^2}+\frac{1}{r}\frac{\partial\omega}{\partial r}+\frac{1}{r^2}\frac{\partial^2\omega}{\partial\theta^2}=Re\left(u\frac{\partial\omega}{\partial r}+\frac{v}{r}\frac{\partial\omega}{\partial\theta}+\frac{\partial\omega}{\partial t}\right), \tag{1}$$

$$\frac{\partial^2\psi}{\partial r^2}+\frac{1}{r}\frac{\partial\psi}{\partial r}+\frac{1}{r^2}\frac{\partial^2\psi}{\partial\theta^2}=-\omega. \tag{2}$$

Here ψ is the streamfunction, ω the vorticity, u, v, respectively are the radial and tangential velocity components, t is the time and $Re=\frac{UD}{\nu}$ is the Reynolds number with U being the characteristic velocity, D the diameter of the cylinder and ν the kinematic viscosity. The velocities u and v in terms of ψ are given by

$$u=\frac{1}{r}\frac{\partial\psi}{\partial\theta}\quad\text{and}\quad v=-\frac{\partial\psi}{\partial r}, \tag{3}$$

and the vorticity ω is given by

$$\omega=\frac{1}{r}\left[\frac{\partial}{\partial r}(vr)-\frac{\partial u}{\partial\theta}\right]. \tag{4}$$

We assume the cylinder to be of unit radius placed in an infinite domain. At the far-field, a potential flow is assumed [36] with uniform free-stream velocity $U_\infty=1$. Thus

$$(u_\infty(r,\theta),v_\infty(r,\theta))=\left(U_\infty\left(1-\frac{R_0^2}{r^2}\right)\cos\theta,-U_\infty\left(1+\frac{R_0^2}{r^2}\right)\sin\theta\right). \tag{5}$$

The initial and the boundary conditions are as follows:

$$\omega(r,\theta,0)=0, R_0\leqslant r<\infty,\quad 0\leqslant\theta\leqslant 2\pi, \tag{6}$$

$$(u(r,\theta,t),v(r,\theta,t))=(u_\infty(r,\theta),v_\infty(r,\theta)), r\to\infty,\quad 0\leqslant\theta\leqslant 2\pi. \tag{7}$$

On the surface of the cylinder $r=R_0, 0\leqslant\theta\leqslant 2\pi$

$$(u(r,\theta,t),v(r,\theta,t))=(0,0). \tag{8}$$

The boundary conditions for ψ on the surface of the cylinder can be derived from those of the velocities in (8) as

$$\psi(r,\theta)=0,\quad \frac{\partial\psi}{\partial r}(r,\theta)=0,\quad 0\leqslant\theta\leqslant 2\pi. \tag{9}$$

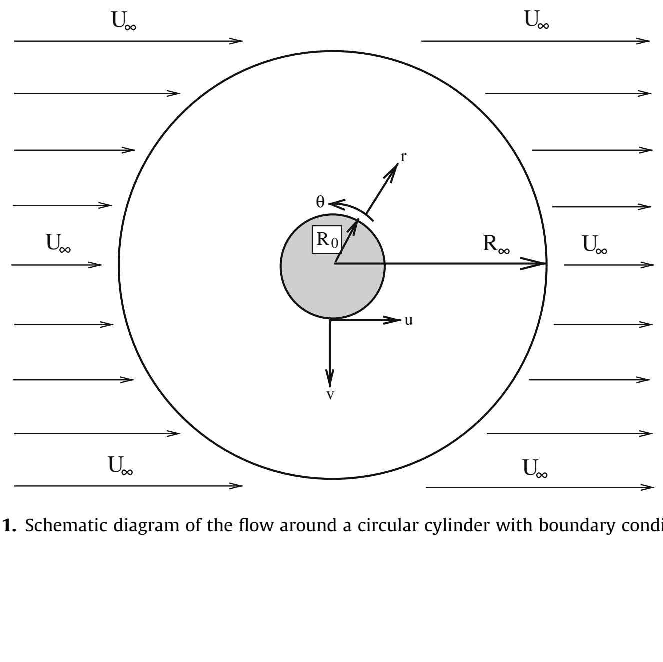

Fig. 1. Schematic diagram of the flow around a circular cylinder with boundary conditions.

At the far field where $r \to \infty$,

$$\psi(r,\theta) = \left(r - \frac{R_0^2}{r}\right)\sin\theta, \quad \frac{\partial\psi}{\partial r}(r,\theta) = \left(1 + \frac{R_0^2}{r^2}\right)\sin\theta, \quad 0 \leqslant \theta \leqslant 2\pi. \tag{10}$$

3. Discretization and mathematical formulation

3.1. The numerical scheme

As the title of our paper suggests, we are interested in computing the incompressible viscous flows past a circular cylinder where the computational and physical planes are the same. We construct a nonuniform polar mesh (see a typical stencil at the n or $(n+1)$th time level in Fig. 2) in the annular region $\Omega = [R_0, R_\infty] \times [0, 2\pi]$ by the points (r_i, θ_j) which are not necessarily equally spaced. At a typical (i,j)th node, the forward and backward step lengths in the r-direction are given by $r_f = (r_{i+1} - r_i), r_b = (r_i - r_{i-1})$, respectively. Similarly in the θ-direction, $\theta_f = (\theta_{j+1} - \theta_j), \theta_b = (\theta_j - \theta_{j-1})$. Assuming the stream-function ψ to be smooth, the finite difference approximations of first and second derivatives appearing in (2) at the (i,j)th node are given [5] as follows:

$$\left.\frac{\partial\psi}{\partial r}\right|_{i,j} = \delta_r\psi_{i,j} - \frac{1}{2}(r_f - r_b)\delta_r^2\psi_{i,j} - \frac{r_f r_b}{6}\left.\frac{\partial^3\psi}{\partial r^3}\right|_{i,j} - \frac{1}{24}r_f r_b(r_f - r_b)\left.\frac{\partial^4\psi}{\partial r^4}\right|_{i,j} + O\left(\frac{r_f^5 + r_b^5}{r_f + r_b}\right), \tag{11}$$

$$\left.\frac{\partial^2\psi}{\partial r^2}\right|_{i,j} = \delta_r^2\psi_{i,j} - \frac{1}{3}(r_f - r_b)\left.\frac{\partial^3\psi}{\partial r^3}\right|_{i,j} - \frac{1}{12}\left(r_f^2 + r_b^2 - r_f r_b\right)\left.\frac{\partial^4\psi}{\partial r^4}\right|_{i,j} - \frac{1}{60}(r_f - r_b)(r_f^2 + r_b^2)\left.\frac{\partial^5\psi}{\partial r^5}\right|_{i,j} + O\left(\frac{r_f^5 + r_b^5}{r_f + r_b}\right). \tag{12}$$

The derivatives with respect to θ can be obtained in a similar way; here, δ_r, δ_θ and $\delta_r^2, \delta_\theta^2$ are the first and second order nonuniform central difference operators in the r and θ-directions, respectively. The procedure for approximating the derivatives of ω is the same. In view of the above equations, Eqs. (1) and (2) may be approximated at the (i,j)th point as

$$\left[\delta_r^2 + \frac{1}{r_i^2}\delta_\theta^2 + c_1\{\delta_r - 0.5(r_f - r_b)\delta_r^2\} - d_1\{\delta_\theta - 0.5(\theta_f - \theta_b)\delta_\theta^2\}\right]\omega_{i,j} - (\tau_1)_{i,j} = Re\left(\frac{\partial\omega}{\partial t}\right)_{i,j} \tag{13}$$

$$\left[\delta_r^2 + \frac{1}{r_i^2}\delta_\theta^2 + \frac{1}{r_i}\{\delta_r - 0.5(r_f - r_b)\delta_r^2\}\right]\psi_{i,j} - (\tau_2)_{i,j} = -\omega_{i,j}, \tag{14}$$

respectively, where,

$$c_1 = \frac{1}{r_i} - Re\, u_{i,j}, \quad d_1 = \frac{Re\, v_{i,j}}{r_i}$$

$$(\tau_1)_{i,j} = H_{11}\frac{\partial^3\omega}{\partial r^3} + K_{11}\frac{\partial^3\omega}{\partial\theta^3} + H_{12}\frac{\partial^4\omega}{\partial r^4} + K_{12}\frac{\partial^4\omega}{\partial\theta^4} + (r_f - r_b)\left(r_f^2 + r_b^2\right)\phi_{11} + (\theta_f - \theta_b)\left(\theta_f^2 + \theta_b^2\right)\phi_{12} + O\left(\frac{r_f^5 + r_b^5}{r_f + r_b}, \frac{\theta_f^5 + \theta_b^5}{\theta_f + \theta_b}\right), \tag{15}$$

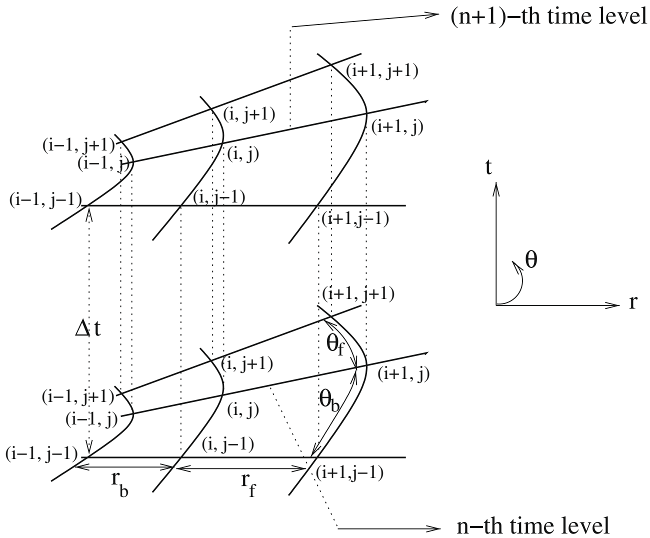

Fig. 2. The unsteady HOC stencil on nonuniform polar grid.

$$(\tau_2)_{i,j} = H_{21}\frac{\partial^3\psi}{\partial r^3} + K_{21}\frac{\partial^3\psi}{\partial\theta^3} + H_{22}\frac{\partial^4\psi}{\partial r^4} + K_{22}\frac{\partial^4\psi}{\partial\theta^4} + (r_f - r_b)\left(r_f^2 + r_b^2\right)\phi_{21} + (\theta_f - \theta_b)\left(\theta_f^2 + \theta_b^2\right)\phi_{22} + O\left(\frac{r_f^5 + r_b^5}{r_f + r_b}, \frac{\theta_f^5 + \theta_b^5}{\theta_f + \theta_b}\right), \quad (16)$$

with $\phi_{11}, \phi_{12}, \phi_{21}, \phi_{22}$ being the leading truncation error terms and

$$H_{11} = \frac{1}{6}\{2(r_f - r_b) + cr_f r_b\}, \quad H_{12} = \frac{1}{24}\left\{2\left(r_f^2 + r_b^2 - r_f r_b\right) + cr_f r_b(r_f - r_b)\right\},$$
$$K_{11} = \frac{1}{6}\left\{\frac{2}{r_i^2}(\theta_f - \theta_b) - d\theta_f\theta_b\right\}, \quad K_{12} = \frac{1}{24}\left\{\frac{2}{r_i^2}\left(\theta_f^2 + \theta_b^2 - \theta_f\theta_b\right) - d\theta_f\theta_b(\theta_f - \theta_b)\right\},$$
$$H_{21} = \frac{1}{6}\{2(r_f - r_b) + \frac{r_f r_b}{r_i}\}, \quad H_{22} = \frac{1}{24}\left\{2\left(r_f^2 + r_b^2 - r_f r_b\right) + \frac{r_f r_b}{r_i}(r_f - r_b)\right\},$$
$$K_{21} = \frac{1}{3r_i^2}(\theta_f - \theta_b), \quad K_{22} = \frac{1}{12r_i^2}\left(\theta_f^2 + \theta_b^2 - \theta_f\theta_b\right).$$

To obtain a higher order spatial compact finite difference approximation (at least up to third order spatial accuracy on non-uniform grids) for (1) and (2), the third and fourth order derivatives appearing in τ_1 and τ_2 are compactly approximated [5] to at least second order spatial accuracy. In order to accomplish this, the original equations (1) and (2) are treated as auxiliary relations that can be differentiated to obtain higher order derivatives. For example, successive differentiation of (1) with respect to r and θ and rearranging terms yield

$$\frac{\partial^3\omega}{\partial r^3} = \left(Reu - \frac{1}{r}\right)\frac{\partial^2\omega}{\partial r^2} + \left(Reu_r + \frac{1}{r^2}\right)\frac{\partial\omega}{\partial r} + \frac{Re\,v}{r}\frac{\partial^2\omega}{\partial r\partial\theta} - \frac{1}{r^2}\frac{\partial^3\omega}{\partial r\partial\theta^2} + \left(\frac{Re\,v_r r - Re\,v}{r^2}\right)\frac{\partial\omega}{\partial\theta} + \frac{2}{r^3}\frac{\partial^2\omega}{\partial\theta^2} + Re\frac{\partial}{\partial r}\left(\frac{\partial\omega}{\partial t}\right), \quad (17)$$

$$\frac{\partial^4\omega}{\partial r^4} = T_1\frac{\partial^2\omega}{\partial r^2} + T_2\frac{\partial\omega}{\partial r} + T_3\frac{\partial^2\omega}{\partial r\partial\theta} + T_4\frac{\partial^3\omega}{\partial r\partial\theta^2} + \frac{Re\,v}{r}\frac{\partial^3\omega}{\partial r^2\partial\theta} - \frac{1}{r^2}\frac{\partial^4\omega}{\partial r^2\partial\theta^2} + T_5\frac{\partial\omega}{\partial\theta} + T_6\frac{\partial^2\omega}{\partial\theta^2} + \left(Reu - \frac{1}{r}\right)Re\frac{\partial}{\partial r}\left(\frac{\partial\omega}{\partial t}\right) + Re\frac{\partial^2}{\partial r^2}\left(\frac{\partial\omega}{\partial t}\right), \quad (18)$$

where,

$$T_1 = \left(Reu - \frac{1}{r}\right)^2 + 2\left(Reu_r + \frac{1}{r^2}\right), \quad T_2 = \left(Reu - \frac{1}{r}\right)\left(Reu_r + \frac{1}{r^2}\right) + \left(Reu_{rr} - \frac{2}{r^3}\right),$$
$$T_3 = \left(Reu - \frac{1}{r}\right)\frac{Re\,v}{r} + 2\left(\frac{Re\,v_r r - Re\,v}{r^2}\right), \quad T_4 = \frac{4}{r^3} - \left(Reu - \frac{1}{r}\right)\frac{1}{r^2}$$
$$T_5 = \left(Reu - \frac{1}{r}\right)\left(\frac{Re\,v_r r - Re\,v}{r^2}\right) + \left(\frac{Re\,v_{rr}r^2 - 2Re\,v_r r + 2Re\,v}{r^3}\right),$$
$$T_6 = \left(Reu - \frac{1}{r}\right)\frac{2}{r^3} - \frac{6}{r^4}.$$

and

$$\frac{\partial^3\omega}{\partial\theta^3} = Re\,vr\frac{\partial^2\omega}{\partial\theta^2} + Re\,v_\theta r\frac{\partial\omega}{\partial\theta} + (Reur^2 - r)\frac{\partial^2\omega}{\partial r\partial\theta} - r^2\frac{\partial^3\omega}{\partial r^2\partial\theta} + Reu_\theta r^2\frac{\partial\omega}{\partial r} + Rer^2\frac{\partial}{\partial\theta}\left(\frac{\partial\omega}{\partial t}\right),$$

$$\frac{\partial^4\omega}{\partial\theta^4} = \{(Re\,vr)^2 + 2Re\,v_\theta r\}\frac{\partial^2\omega}{\partial\theta^2} + (Re^2 v_\theta vr^2 + Re\,v_{\theta\theta}r)\frac{\partial\omega}{\partial\theta} + \{Re\,vr(Reur^2 - r) + 2Reu_\theta r^2\}\frac{\partial^2\omega}{\partial r\partial\theta} - Re\,vr^3\frac{\partial^3\omega}{\partial r^2\partial\theta} - r^2\frac{\partial^4\omega}{\partial r^2\partial\theta^2} + (Reur^2 - r)\frac{\partial^3\omega}{\partial r\partial\theta^2} + (Re^2 u_\theta vr^3 + Reu_{\theta\theta}r^2)\frac{\partial\omega}{\partial r} + Re^2 vr^3\frac{\partial}{\partial\theta}\left(\frac{\partial\omega}{\partial t}\right) + Rer^2\frac{\partial^2}{\partial\theta^2}\left(\frac{\partial\omega}{\partial t}\right).$$

Expressions for the higher order spatial derivatives of ω can be found in a similar way. The approximations for the mixed derivatives such as $\frac{\partial^3\omega}{\partial r^2\partial\theta}, \frac{\partial^3\omega}{\partial r\partial\theta^2}$ and $\frac{\partial^4\omega}{\partial r^2\partial\theta^2}$ can be found out by the successive applications of the approximations for the first and second derivatives given in (11) and (12). Note that all the derivatives appearing in τ_1 and τ_2 being approximated are of the form $\frac{\partial^{p+q}\omega}{\partial r^p\partial\theta^q}$ where $p, q \leqslant 2$. Therefore the central difference approximations of these derivatives do not extend beyond one mesh length away from the point about which the finite differences are taken. As a result of this, the HOC computational stencil is always restricted to a maximum of nine points as shown in Fig. 2. Once all the approximations are substituted for the derivatives, the spatially HOC approximations of Eqs. (1) and (2) can be written as

$$\left[A1_{i,j}\delta_r^2 + A2_{i,j}\delta_\theta^2 + A3_{i,j}\delta_r + A4_{i,j}\delta_\theta + A5_{i,j}\delta_r\delta_\theta + A6_{i,j}\delta_r\delta_\theta^2 + A7_{i,j}\delta_r^2\delta_\theta + A8_{i,j}\delta_r^2\delta_\theta^2\right]\omega_{i,j} = F_{i,j} \quad (19)$$

and

$$\left[B1_{i,j}\delta_r^2 + B2_{i,j}\delta_\theta^2 + B3_{i,j}\delta_r + B4_{i,j}\delta_r\delta_\theta + B5_{i,j}\delta_r\delta_\theta^2 + B6_{i,j}\delta_r^2\delta_\theta + B7_{i,j}\delta_r^2\delta_\theta^2\right]\psi_{i,j} = G_{i,j}, \quad (20)$$

respectively, where the coefficients are given by

$$
\begin{aligned}
A1_{i,j} &= 1 - 0.5c_1(r_f - r_b) - (H_{12}c_1^2 - c_1H_{11}) - 2H_{12}\left(Re(u_r)_{i,j} + \frac{1}{r_i^2}\right),\\
B1_{i,j} &= 1 - \frac{(r_f - r_b)}{2r_i} + (r_iH_{21} - H_{22})\frac{1}{r_i^2} - \frac{2H_{22}}{r_i^3},\\
A2_{i,j} &= \frac{1}{r_i^2} + 0.5d_1(\theta_f - \theta_b) - \frac{2}{r_i^3}(H_{11} - H_{12}c_1) + \frac{6H_{12}}{r_i^4} - Re\,v_{i,j}r_i(K_{11} + Re\,v_{i,j}r_iK_{12}) - 2K_{12}Re(v_\theta)_{i,j}r_i,\\
B2_{i,j} &= \frac{1}{r_i^2} - (r_iH_{21} - H_{22})\frac{2}{r_i^4} + \frac{6H_{22}}{r_i^4},\\
A3_{i,j} &= c_1 - (H_{11} - c_1H_{12})\left(Re(u_r)_{i,j} + \frac{1}{r_i^2}\right) - H_{12}\left(Re(u_{rr})_{i,j} - \frac{2}{r_i^3}\right)\\
&\quad - Re(u_\theta)_{i,j}r_i^2(K_{11} + Re\,v_{i,j}r_iK_{12}) - K_{12}Re(v_{\theta\theta})_{i,j}r_i^2,\\
B3_{i,j} &= \frac{1}{r_i} - (r_iH_{21} - H_{22})\frac{1}{r_i^3} + \frac{2H_{22}}{r_i^3},\\
A4_{i,j} &= -d_1 - (H_{11} - c_1H_{12})((v_r)_{i,j}r_i - v_{i,j})\frac{Re}{r_i^2} - H_{12}\left((v_{rr})_{i,j}r_i^2 - 2(v_r)_{i,j}r_i + 2v_{i,j}\right)\frac{Re}{r_i^3}\\
&\quad - Re(v_\theta)_{i,j}r_i(K_{11} + Re\,v_{i,j}r_iK_{12}) - K_{12}Re(v_{\theta\theta})_{i,j}r_i,\\
B4_{i,j} &= r_iK_{21},\\
A5_{i,j} &= -d_1(H_{11} - c_1H_{12}) - 2H_{12}((v_r)_{i,j}r_i - v_{i,j})\frac{Re}{r_i^2} + c_1r_i^2(K_{11} + Re\,v_{i,j}r_iK_{12}) - 2K_{12}Re(v_\theta)_{i,j}r_i^2,\\
B5_{i,j} &= (r_iH_{21} - H_{22})\frac{1}{r_i^3} - \frac{4H_{22}}{r_i^3} + r_iK_{22},\\
A6_{i,j} &= (H_{11} - c_1H_{12})\frac{1}{r_i^2} - \frac{4H_{12}}{r_i^3} + c_1K_{12}r_i^2,\\
B6_{i,j} &= r_i^2K_{21},\\
A7_{i,j} &= -d_1H_{12} + r_i^2(K_{11} + Re\,v_{i,j}r_iK_{12}),\\
B7_{i,j} &= \frac{H_{22}}{r_i^2} + r_i^2K_{22},\\
A8_{i,j} &= \frac{H_{12}}{r_i^2} + K_{12}r_i^2,\\
F_{i,j} &= \left[Re + Re(H_{11} - c_1H_{12})\delta_r + H_{12}Re\delta_r^2 + Rer_i^2(K_{11} + Re\,v_{i,j}r_iK_{12})\delta_\theta + K_{12}Rer_i^2\delta_\theta^2\right]\frac{\partial\omega}{\partial t},\\
G_{i,j} &= -\left[1 + (r_iH_{21} - H_{22})\frac{1}{r_i}\delta_r + H_{22}\delta_r^2 + K_{21}r_i^2\delta_\theta + K_{22}r_i^2\delta_\theta^2\right]\omega_{i,j}.
\end{aligned}
$$

The details of all the spatial finite difference operators appearing in Eqs. (19) and (20) can be found in the appendix.

Note that the expression F_{ij} in Eq. (19) has a temporal derivative term $\frac{\partial\omega}{\partial t}$. We use forward difference to discretize this term and then a weighted average parameter value of $\frac{1}{2}$ for this derivative [4,6,47] to arrive at a Crank–Nicolson type of approximation for Eq. (19)

$$
\begin{aligned}
&\left[A11_{i,j}\delta_r^2 + A12_{i,j}\delta_\theta^2 + A13_{i,j}\delta_r + A14_{i,j}\delta_\theta + A15_{i,j}\delta_r\delta_\theta + A16_{i,j}\delta_r\delta_\theta^2 + A17_{i,j}\delta_r^2\delta_\theta + A18_{i,j}\delta_r^2\delta_\theta^2\right]\omega_{i,j}^{n+1}\\
&\quad = \left[A21_{i,j}\delta_r^2 + A22_{i,j}\delta_\theta^2 + A23_{i,j}\delta_r + A24_{i,j}\delta_\theta + A25_{i,j}\delta_r\delta_\theta + A26_{i,j}\delta_r\delta_\theta^2 + A27_{i,j}\delta_r^2\delta_\theta + A28_{i,j}\delta_r^2\delta_\theta^2\right]\omega_{i,j}^{n},
\end{aligned}
\tag{21}
$$

where,

$$
\begin{aligned}
&A11_{i,j} = (H_{12}Re - 0.5\Delta tA1_{i,j}), \quad A21_{i,j} = (H_{12}Re + 0.5\Delta tA1_{i,j}),\\
&A12_{i,j} = (r_i^2K_{12}Re - 0.5\Delta tA2_{i,j}), \quad A22_{i,j} = (r_i^2K_{12}Re + 0.5\Delta tA2_{i,j}),\\
&A13_{i,j} = (Re(H_{11} - c_1H_{12}) - 0.5\Delta tA3_{i,j}), \quad A23_{i,j} = (Re(H_{11} - c_1H_{12}) + 0.5\Delta tA3_{i,j}),\\
&A14_{i,j} = (r_i^2Re(K_{11} + r_iRe\,v_{i,j}K_{12}) - 0.5\Delta tA4_{i,j}),\\
&A24_{i,j} = (r_i^2Re(K_{11} + r_iRe\,v_{i,j}K_{12}) + 0.5\Delta tA4_{i,j}),\\
&A15_{i,j} = -0.5\Delta tA5_{i,j}, \quad A25_{i,j} = 0.5\Delta tA5_{i,j},\\
&A16_{i,j} = -0.5\Delta tA6_{i,j}, \quad A26_{i,j} = 0.5\Delta tA6_{i,j},\\
&A17_{i,j} = -0.5\Delta tA7_{i,j}, \quad A27_{i,j} = 0.5\Delta tA7_{i,j},\\
&A18_{i,j} = -0.5\Delta tA8_{i,j}, \quad A28_{i,j} = 0.5\Delta tA8_{i,j}.
\end{aligned}
$$

Thus (21) is the HOC approximation of the vorticity equation (1) which is at least third order accurate in space and second order accurate in time; likewise, (20) is the approximation of the streamfunction equation (2). It may be noted that on a uniform grid the spatial accuracy of both (20) and (21) becomes four.

3.2. Approximation of the boundary conditions

The numerical implementation of the boundary conditions for u, v and ψ are straightforward. The vorticity ω at the far field is zero. It may be noted that for computational purpose we fix r as R_∞ at the far field. At the solid boundary, making use of Eqs. (2) and (9), for all θ at $r = R_0$, we have

$$\omega = -\frac{\partial^2 \psi}{\partial r^2} \tag{22}$$

thereat. We proceed to obtain a compact approximation of the vorticity on the solid boundary as follows:

Employing a Taylor series expansion, we get

$$0 = -\frac{\partial \psi}{\partial r}\bigg|_{0,j} = -\delta_r \psi_{0,j} + \frac{r_f}{2}\frac{\partial^2 \psi}{\partial r^2}\bigg|_{0,j} + \frac{r_f^2}{6}\frac{\partial^3 \psi}{\partial r^3}\bigg|_{0,j} + \frac{r_f^3}{24}\frac{\partial^4 \psi}{\partial r^4}\bigg|_{0,j} + O\left(r_f^4\right) \tag{23}$$

Using (22) in (23), we get the fourth order accurate expression

$$0 = -\delta_r \psi_{0,j} - \left(\frac{r_f \omega_{0,j}}{2} + \frac{r_f^2}{6}\frac{\partial \omega}{\partial r} + \frac{r_f^3}{24}\frac{\partial^2 \omega}{\partial r^2}\right)\bigg|_{0,j} + O\left(r_f^4\right) \tag{24}$$

Making use of the fact that on the solid wall $u = 0,\ v = 0$, Eq. (1) yields,

$$\frac{\partial^2 \omega}{\partial r^2} = Re\frac{\partial \omega}{\partial t} - \frac{1}{r_0}\frac{\partial \omega}{\partial r} - \frac{1}{r_0^2}\frac{\partial^2 \omega}{\partial \theta^2} \tag{25}$$

Using (25) in (24) and after some simplifications we get,

$$0 = -\delta_r \psi_{0,j} - \frac{r_f}{2}\omega_{0,j} + \left(\frac{r_f^3}{24 r_0} - \frac{r_f^2}{6}\right)\frac{\partial \omega}{\partial r}\bigg|_{0,j} - \frac{r_f^3 Re}{24}\frac{\partial \omega}{\partial t}\bigg|_{0,j} + \frac{r_f^3}{24 r^2}\frac{\partial^2 \omega}{\partial \theta^2}\bigg|_{0,j}. \tag{26}$$

Using forward difference for the temporal derivative and second order one-sided difference for the derivatives along r-direction, we finally get

$$\begin{aligned}\omega_{0,j}^{n+1} = \frac{24\Delta t}{r_f^3 Re}\Bigg[&\left\{\frac{r_f^3 Re}{24\Delta t} - \frac{r_f}{2} - \left(\frac{r_f^3}{24 r_0} - \frac{r_f^2}{6}\right)\left(\frac{(r_2 - r_0)^2 - r_f^2}{r_f(r_2 - r_0)(r_2 - r_1)}\right) - \frac{r_f^3}{24 r_0^2 \Delta\theta}\left(\frac{1}{\theta_f} + \frac{1}{\theta_f}\right)\right\}\omega_{0,j}^n \\ &+ \frac{r_f^3}{24 r_0^2 \theta_b \Delta\theta}\omega_{0,j-1}^n \frac{r_f^3}{24 r_0^2 \theta_f \Delta\theta}\omega_{0,j+1}^n + \left(\frac{r_f^3}{24 r_0} - \frac{r_f^2}{6}\right)\left(\frac{(r_2 - r_0)^2 \omega_{1,j}^n - r_f^2 \omega_{2,j}^n}{r_f(r_2 - r_0)(r_2 - r_1)}\right)\Bigg].\end{aligned} \tag{27}$$

3.3. Calculation of drag and lift coefficients

In the case of viscous flows for bluff bodies immersed in fluids, the forces that are being exerted on the body come from surface pressure distribution and surface friction. The surface pressure distribution can be calculated from the tangential momentum equation at the surface of the body. To calculate the lift (C_L) and drag coefficients (C_D), we use the following formulas [39,44], respectively,

$$C_L = \frac{1}{Re}\int_0^{2\pi}\left[\left(\frac{\partial \omega}{\partial r}\right)_{R_0} - \omega_{R_0}\right] cos\theta d\theta, \tag{28}$$

$$C_D = \frac{1}{Re}\int_0^{2\pi}\left[\left(\frac{\partial \omega}{\partial r}\right)_{R_0} - \omega_{R_0}\right] sin\theta d\theta. \tag{29}$$

The integral over θ along the cylinder is numerically computed using Trapezoidal rule.

3.4. The Grid used

We employ a uniform grid spacing along the θ-direction and nonuniform grid spacing in the r-direction with clustering around the surface of the cylinder using the following functions:

$$\theta_j = \frac{2\pi}{j_{\max}} \text{ and } r_i = \exp\left(\frac{\lambda\pi i}{i_{\max}}\right).$$

Here the parameter λ determines the outer radius of the computational domain. The continuity conditions at $\theta = 0$ and $\theta = 2\pi$ are taken as the boundary conditions along those two lines. A typical computational grid of size 101×101 is shown in Fig. 3.

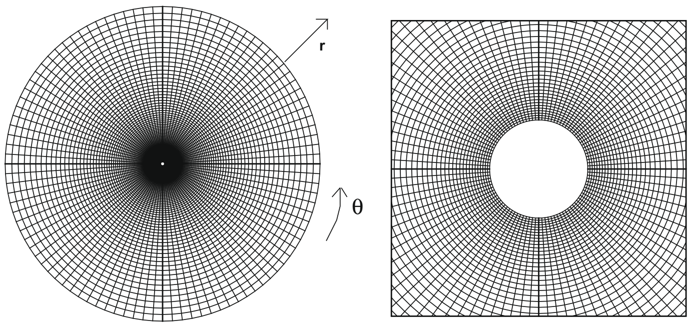

Fig. 3. A typical nonuniform 101×101 mesh with clustering around the cylinder.

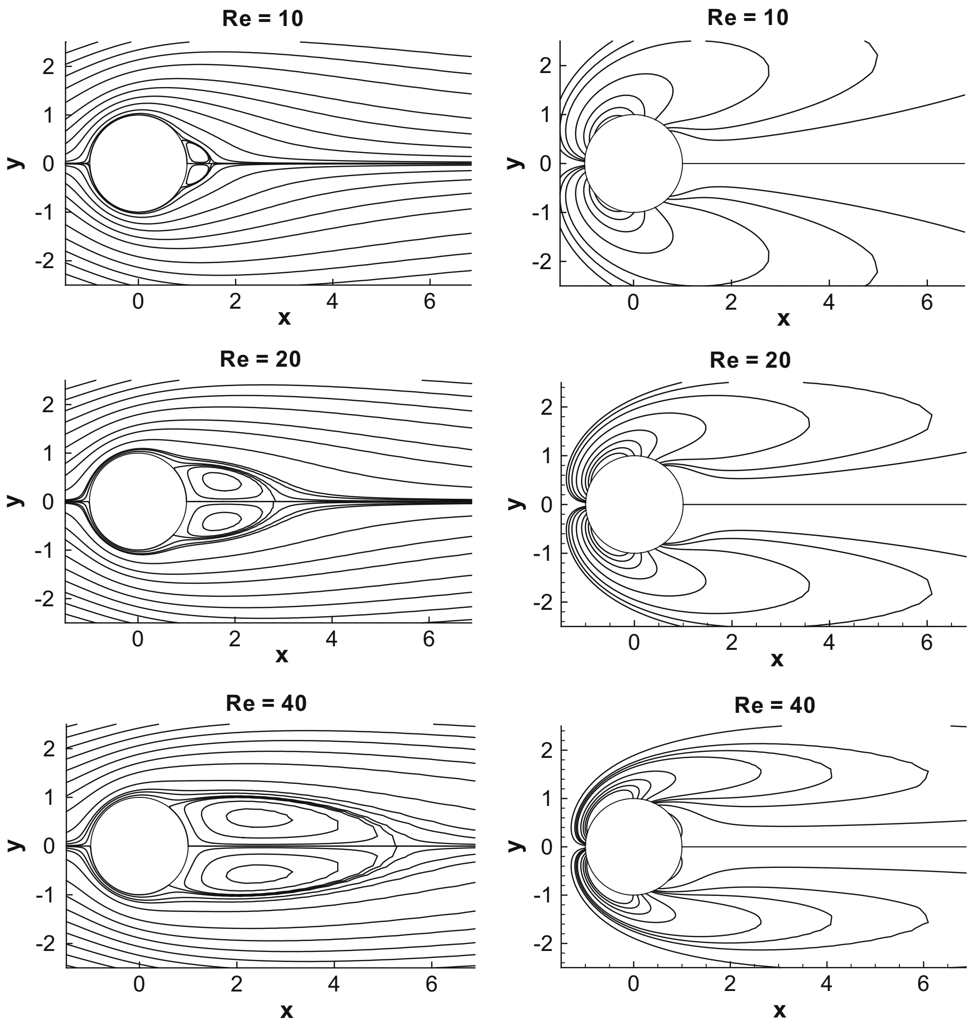

Fig. 4. Steady-state streamlines (left) and vorticity contours (right) for $Re = 10, 20$ and 40 for the motion past a circular cylinder problem.

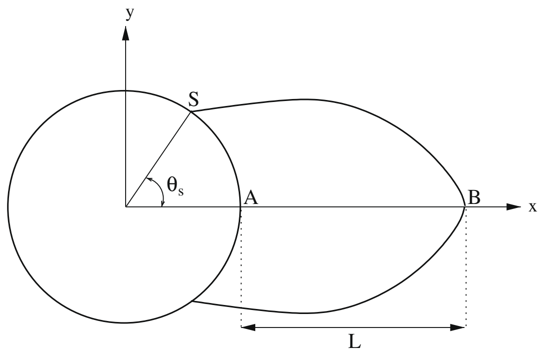

Fig. 5. Geometrical parameters of the closed wake for the motion past a circular cylinder problem.

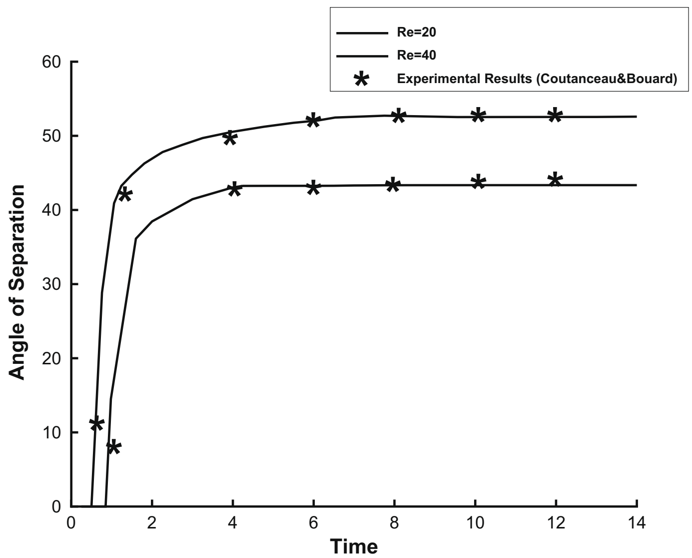

Fig. 6. Comparison of angles of separation for low *Re*s with the results of reference [30] for the motion past a circular cylinder problem.

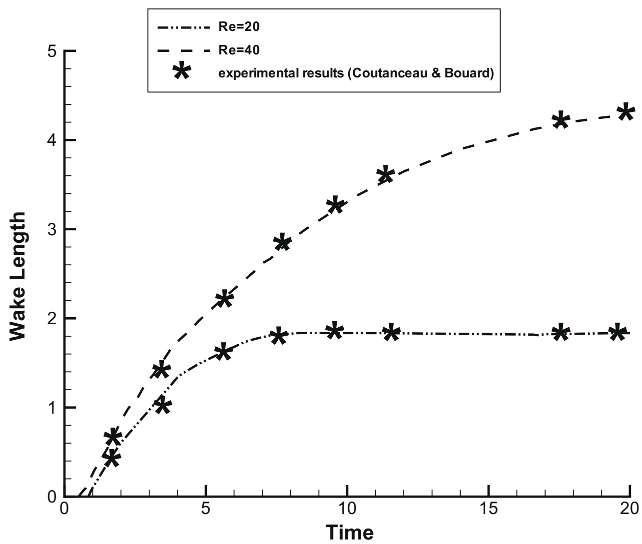

Fig. 7. Comparison of wake length for low *Re*s with the results of reference [30] for the motion past a circular cylinder problem.

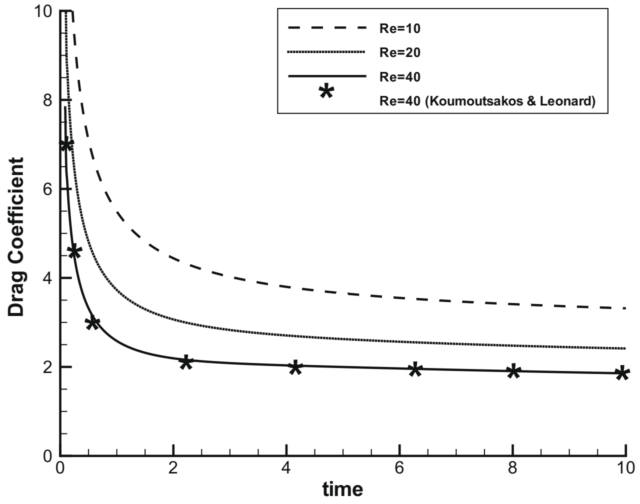

Fig. 8. Comparison of drag coefficient for low *Res* with the results of reference [44] for the motion past a circular cylinder problem.

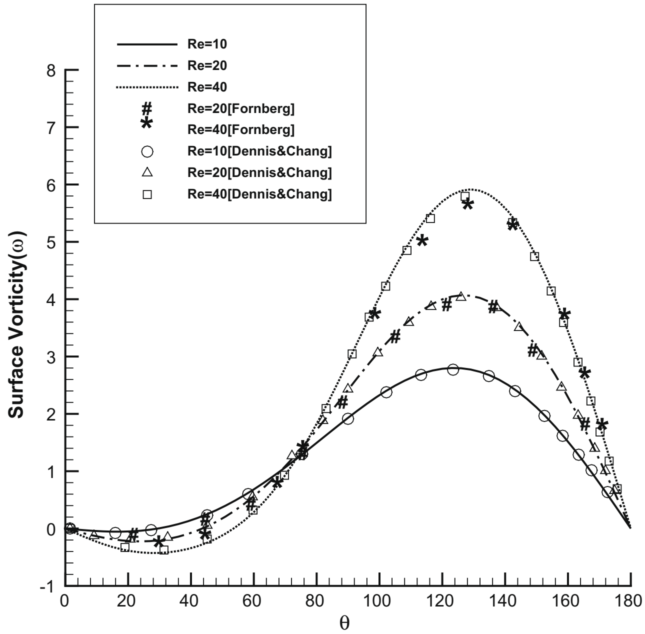

Fig. 9. Comparison of vorticities on the cylinder surface for low *Res* with the results of references [33] and [34] for the motion past a circular cylinder problem.

Table 1
Effect of grid size on wake lengths and separation angles.

	$Re = 20$			$Re = 40$		
Grid	75	101	151	75	101	151
θ_s	42.9248	43.2756	43.4224	51.3012	51.5342	51.7018
L	1.8331	1.8276	1.8226	4.4135	4.3988	4.3921

4. Solution of algebraic systems

We now discuss the solution of algebraic systems associated with the newly proposed finite difference approximations. The system of equations arising out of (20) and (21) can be written as

$$\sum_{k_1=-1}^{1}\sum_{k_2=-1}^{1}\eta 1_{i+k_1,j+k_2}\psi_{i+k_1,j+k_2}=\sum_{k_1=-1}^{1}\sum_{k_2=-1}^{1}\xi 1_{i+k_1,j+k_2}g_{i+k_1,j+k_2}, \tag{30}$$

and

$$\sum_{k_1=-1}^{1}\sum_{k_2=-1}^{1}\eta 2_{i+k_1,j+k_2}\omega^{n+1}_{i+k_1,j+k_2}=\sum_{k_1=-1}^{1}\sum_{k_2=-1}^{1}\xi 2_{i+k_1,j+k_2}\omega^{n}_{i+k_1,j+k_2}, \tag{31}$$

where $\eta 1, \xi 1$ and $\eta 2, \xi 2$'s are functions of the coefficients appearing in the corresponding equations (2) and (1), their derivatives and the step lengths $r_f, r_b, \theta_f, \theta_b$ and Δt. In matrix form, the system of algebraic equations given by (30) or (31) can now be written as

$$A\Phi = B, \tag{32}$$

where the coefficient matrix A is an asymmetric sparse matrix with each row containing at most nine non-zero entries. ϕ is the unknown vector ψ or ω and B is the known (source) term. For a grid of size $m\times n, A$ is of size $mn\times mn$, and Φ and B are mn-component vectors.

The next step now is to solve Eq. (32); as the coefficient matrix A is not generally diagonally dominant, conventional solvers such as Gauss–Seidel cannot be used. On uniform grids in Cartesian coordinates, some of the associated matrices are symmetric and positive definite, which allows algorithms like conjugate-gradient (CG) [1] to be used. As nonuniform grid and variable coefficients of the derivatives appearing in Eqs. (1) and (2) invariably lead to non-symmetric matrices, in order to solve these systems, we use the hybrid biconjugate gradient stabilized method BiCGStab(2) [1] without preconditioning.

It may be noted that for the coupled nonlinear PDEs (such as the $\psi-\omega$ form of the N–S equations), an iterative solution procedure must be adopted to solve the matrix equation of the type (32) at each time step. Both the vorticity (31) and stream function (30) equations are solved using BiCGStab(2) which may be termed inner iterations. We utilize a relaxation parameter γ for the inner iteration cycles for both ω and ψ. For larger values of Reynolds number, we needed smaller values of γ.

All of our computations were carried out on a Pentium 4 based PC with 512 MB RAM. For the inner iterations, the computations were stopped when the norm of the residual vector $\bar{\mathbf{r}} = B - A\Phi$ (ϕ being either ω or ψ) arising out of equation (32) fell below 0.5×10^{-6}. For the cases where steady-state solution is obtained with a time-marching strategy, the steady-state is assumed to reach when the maximum ω-error between two successive time steps is smaller than 0.5×10^{-7}.

5. Results and discussion

We have used the proposed HOC scheme to visualize and analyze the flow patterns for Reynolds numbers ranging from 10 to 9500. Different grid sizes and outflow boundaries are used to capture the gradually increasing complex flow patterns. The flow regime has been divided into four parts depending upon the almost identical flow characteristics observed within each range. In the first part we discuss about the flow structures for $10\leqslant Re\leqslant 40$; available experimental and the numerical results [29–31,33,34,41,43] show that steady-state is possible for this range. In the second part we discuss about the flow

Table 2
Effect of far field boundary on the wake lengths and separation angles.

	$Re = 20$			$Re = 40$		
R_∞	35.03	60.14	75.17	35.03	60.14	75.17
θ_s	43.6248	43.2156	42.9248	51.9612	51.6342	51.3012
L	1.8177	1.8253	1.8331	4.4044	4.4101	4.4135

Table 3
Comparison of the wake lengths, separation angles and drag coefficients for different Reynolds numbers.

	Re	Ref. [33]	Ref. [32]	Ref. [34]	Ref. [37]	Ref. [41]	Present
L	20	1.88	–	1.82	1.842	1.77	1.8331
	40	4.69	–	4.48	4.49	4.21	4.4135
θ_s	20	43.7	–	42.9	42.96	41.3277	42.9248
	40	53.8	–	51.5	52.84	51.0249	51.3012
C_D	20	2.045	2.05	2.001	2.152	2.0597	2.0193
	40	1.522	1.57	1.498	1.499	1.5308	1.5145

structures for $Re = 60$ and 200; here the wake behind the cylinder becomes unstable. Oscillations in the wake grow in amplitude and finally forms a trail of vortices known as von Kármán vortex street. For the next higher Reynolds numbers being discussed here, we consider only the early stage of the flow in the laminar regime. The first of these are $Re = 300$ and

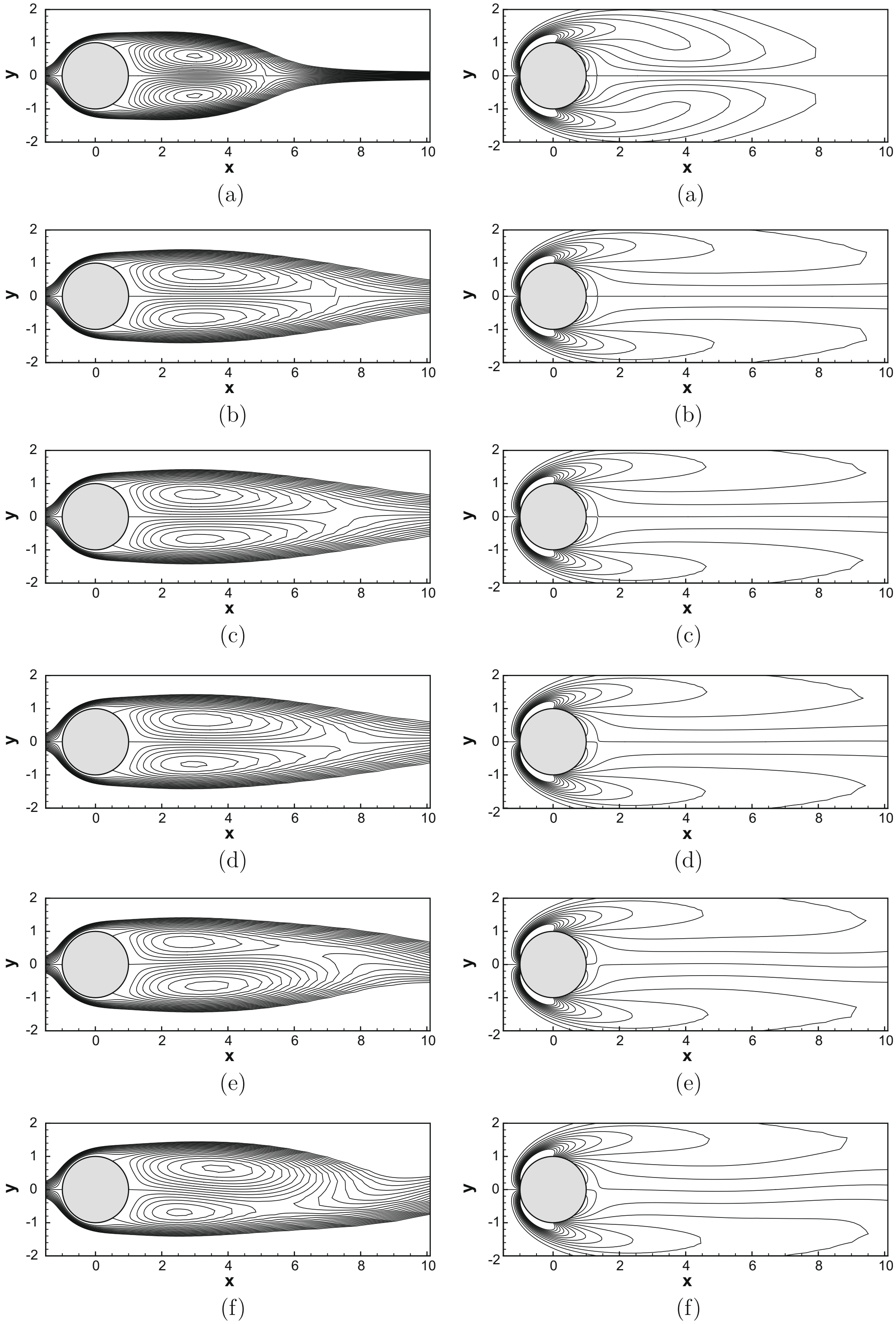

Fig. 10. Streamlines (left) and vorticity contours (right) at $Re = 60$ for flow past a circular cylinder at: (a) $t = 20$, (b) 70, (c) 329, (d) 363, (e) 428 and (f) 468.

550; for these Re, the flow properties are unsteady; secondary vortices develop at the initial stages, but do not split up further. The flow is characterized by the secondary phenomena: (i) bulge phenomenon and (ii) isolated secondary eddy. In the last part, we discuss the range $1000 \leqslant Re \leqslant 9500$ having the most complicated flow properties associated with the so called α- and β-phenomena [31,41,43].

5.1. Flows for $10 \leqslant Re \leqslant 40$

As stated earlier, for the flow past an impulsively started circular cylinder, steady-state is possible up to $Re = 40$. So in this section, we compare our time-marching steady-state results with existing numerical and experimental results [30,32–35,37,41,42,44] for Reynolds numbers $Re = 10,\ 20,$ and 40 in Figs. 4–9 and Tables 1–3.

In Fig. 4, we exhibit the streamlines and vorticity contours from $Re = 10$ to 40. In all the cases, two symmetrical, stationary circulating eddies develop behind the cylinder. With increase in Re values, one can see the increase in the sizes of the vortices.

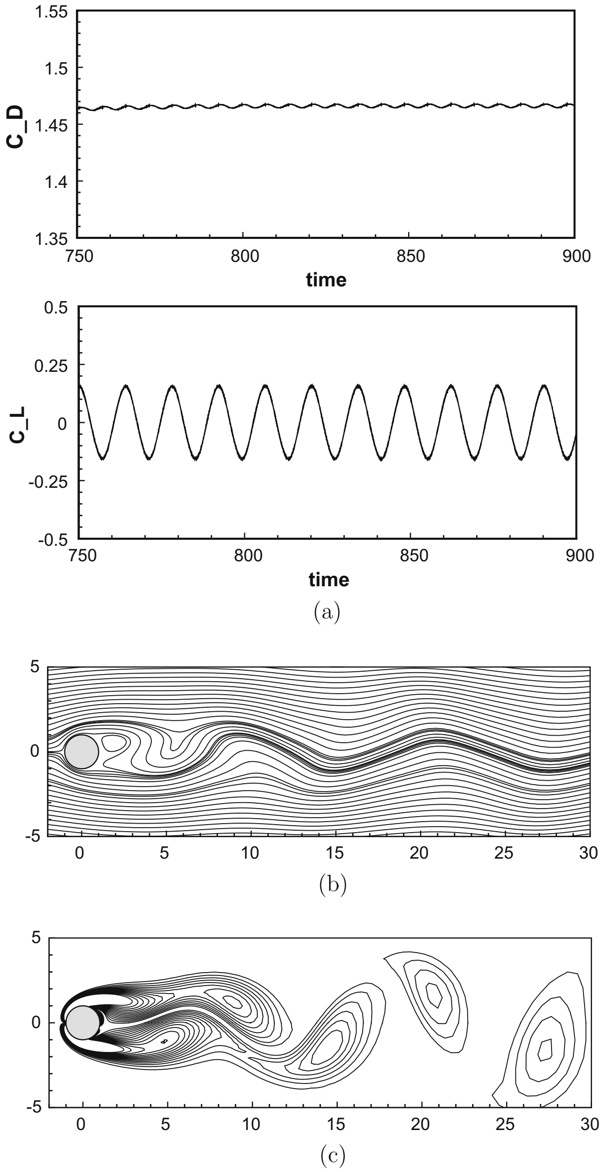

Fig. 11. For $Re = 60$, (a) time history of the drag and lift coefficients, (b) streamline and (b) vorticity contours (corresponding to the peak value of the lift coefficient) for the temporally periodic solution.

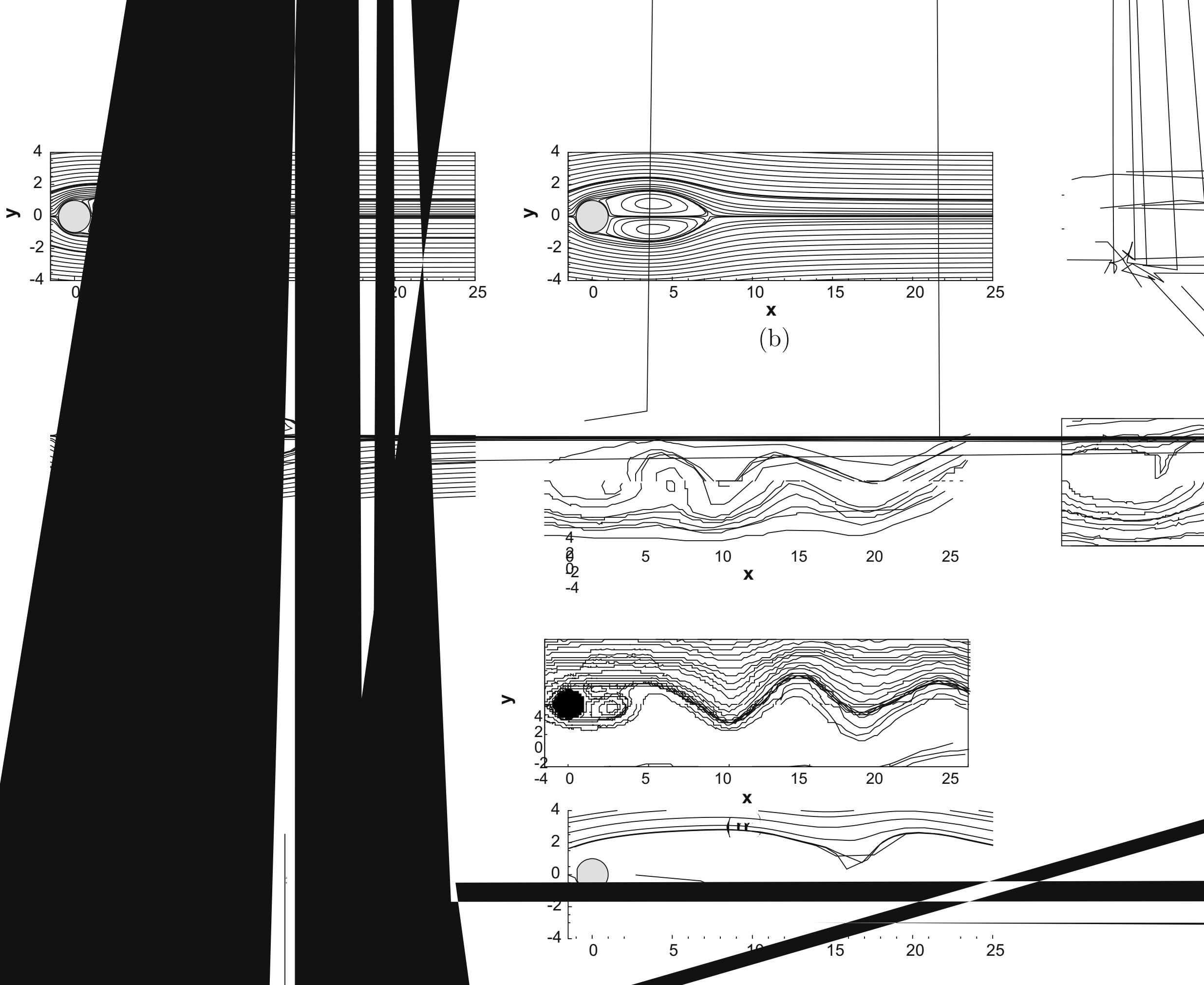

(b)

(h)

We also compute the wake length L: the distance between the rear most point A of the cylinder to the end B of the wake (Fig. 5), and the angle of separation θ_s, which is the angle between the x-axis and the line joining the center of the cylinder and the point of separation S on the cylinder (Fig. 5). These parameters are then compared in Table 1 in order to verify the grid-independence; the grid sizes range from 75×75 to 151×151 ($R_\infty = 75.17$). Table 2 shows the variation of the same parameters to check the dependence of the computed solution on the assumed far-field where R_∞s range from 35.03 to 75.17. Here the grid size has been fixed at 75×75. From these tables, it is clear that a grid of size 101×101 and a far-field given by $R_\infty = 75$ are enough for accurate resolution of the flow. In Table 3, we present our computed L, θ_s and the drag coefficient C_D along with those obtained by [32–34,37,41]. In Figs. 6 and 7, we compare the evolution of the angles of separation and wake lengths at the earlier stages of the flow for $10 \leqslant Re \leqslant 40$ with the results of [30]; Fig. 8 shows the time evolution of the computed drag coefficients in the range $10 \leqslant Re \leqslant 40$ along with those of [44]. We also compare the vorticity values along the surface of the cylinder for the range of Reynolds numbers considered here with those of references [33,34] in Fig. 9. In all the cases, we obtain excellent comparisons with the established numerical and experimental results, both qualitatively and quantitatively.

5.2. Flows for $Re = 60$ and 200

The flow around a impulsively started circular cylinder for $Re = 60$ and 200 eventually becomes periodic and is known to develop vortex shedding represented by the von Kármán vortex street. The basic difference between the flow patterns of this Re range with the previous one is that, the velocities increase with time more rapidly in the recirculating zone and the secondary vortices develop in this region. In these Re values, flow becomes unsteady. Careful flow visualization reveals that the flow in the early stage of development in the laminar wake region is still two-dimensional and symmetric about the axis $\theta = 0$. Therefore, quite a few number of studies [33–36,43] have used only the upper half circular annular region to compute the flow. However use of the complete annular region for computational purpose enabled us to capture the unsteady periodic nature of the flow for $Re = 60$ and 200 as well. For these two Reynolds numbers, we have used a 181×181 grid and R_∞ is taken as around 35 times of the cylinder radius.

In Fig. 10, we show the evolution of streamlines and vorticity contours for $Re = 60$ from $t = 20$ having a symmetric pattern and leading to the onset of asymmetry in the streamlines at a later time around $t = 329$. The asymmetry in vorticity

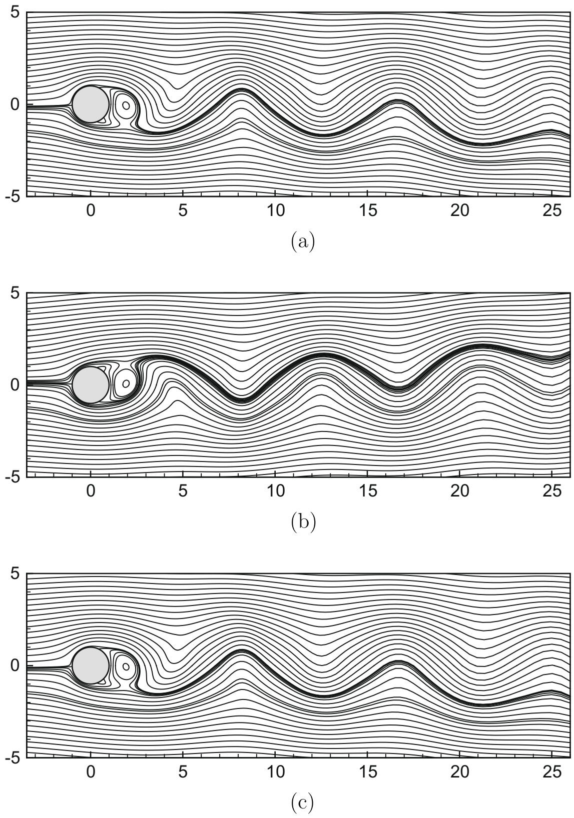

Fig. 13. The streamfunction contours depicting the wake behind three successive instants of time over one vortex shedding period for $Re = 200$. (a) $t = t_0$, (b) $t = t_0 + \frac{T}{2}$ and (c) $t = t_0 + T$.

becomes apparent only when t reaches a value around 428. In Fig. 11(a), we show the time histories of the drag and lift coefficients for $Re = 60$, and in Fig. 11(b) and (c), we show the streamfunction and vorticity fields for the temporally periodic solution corresponding to the peak value of the lift coefficient. Our observations are consistent with ones found in [27]. More

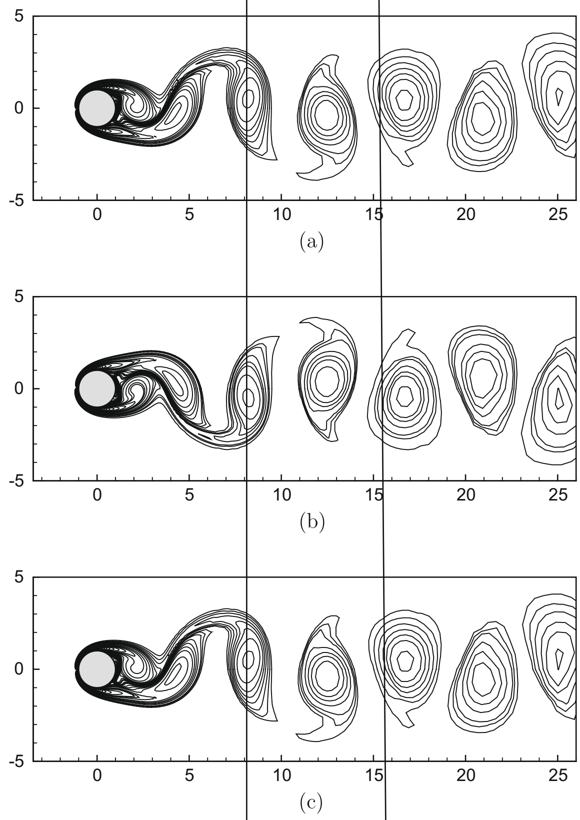

Fig. 14. The vorticity contours depicting the wake behind three successive instants of time over one vortex shedding period for $Re = 200$. (a) $t = t_0$, (b) $t = t_0 + \frac{T}{2}$ and (c) $t = t_0 + T$.

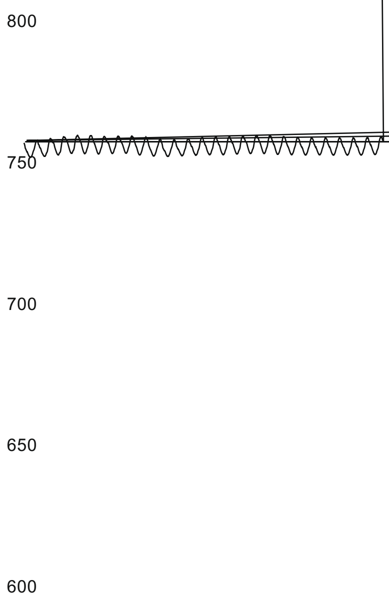

details are presented for the next Reynolds number 200, where we exhibit our numerical results for $Re = 200$ from an early to a periodic stage in Figs. 12–15. In Fig. 12, solution profiles are presented for various values of t till the onset of periodicity. As seen from the figure, a symmetric flow was observed at the beginning (Fig. 12(a)), but the flow became unstable later on, and finally the flow lost its symmetry (Fig. 12(b)–(e)). Eventually, the flow settled into a periodic nature (Fig. 12(n)). We present the temporal evolution of streamlines and vorticity over one complete vortex shedding cycle of duration T in Figs. 13 and 14, respectively. The evolution of an impressive von Kármán vortex street, which is a regular feature for the Reynolds numbers considered here, is clearly seen in these figures.

From Fig. 13, one can see the formation of eddies just behind the cylinder; these eddies are then washed away into the wake region. Two eddies are shed just behind the cylinder within each period (see also Fig. 12(n) and Fig. 13(a)). Fig. 13(a) and (b) are half a vortex shedding cycle apart, and middle Fig. 13(b) is a mirror image of Fig. 13(a) and (c). The corresponding

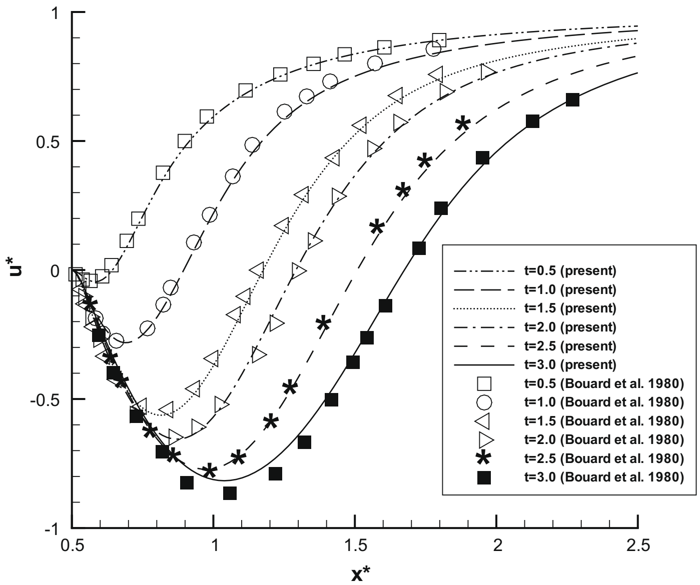

Fig. 16. Radial velocity along the axis of flow for the motion past a circular cylinder for $Re = 200$ at the earlier stages of the flow and comparison with reference [31].

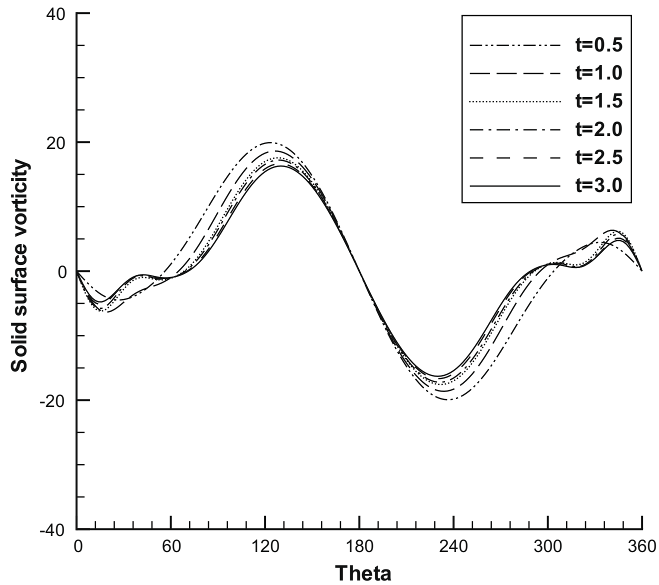

Fig. 17. Vorticity along the solid surface for the motion past a circular cylinder for $Re = 200$ at the earlier stages of the flow.

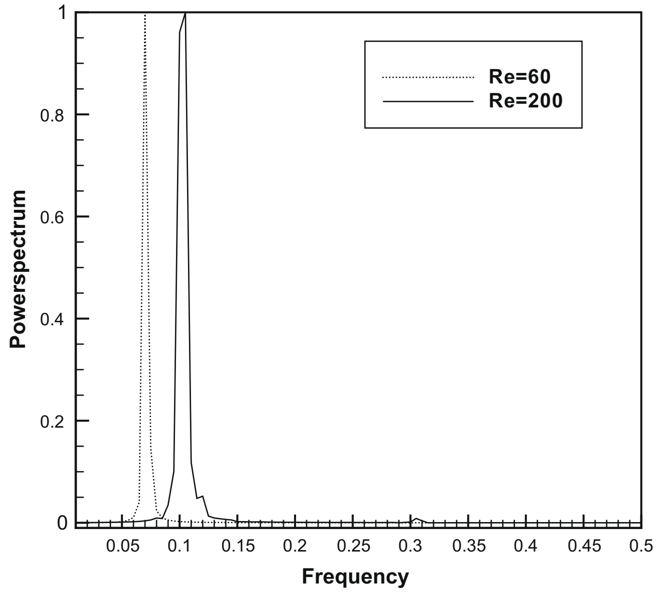

(a)

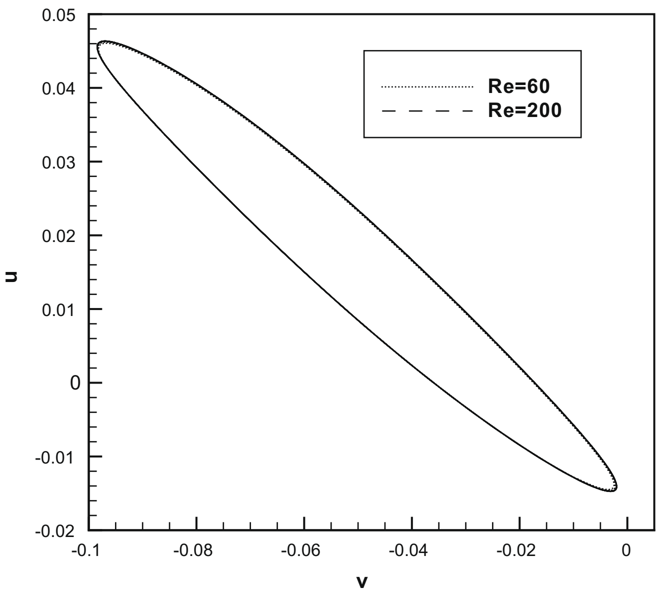

(b)

Fig. 18. Periodic flow for $Re = 60$ and 200: (a) Power spectra of the time series of the lift coefficient, (b) Phase plane trajectories of $u - v$ velocities.

Table 4
Comparison of Strouhal numbers, drag and lift coefficients of the periodic flow for $Re = 60$ and 200.

$Re = 60$				$Re = 200$			
Reference	St	C_D	C_L	Reference	St	C_D	C_L
Williamson (exp.) [53]	0.135			Williamson (exp.) [53]	0.197		
Tritton (exp.) [32]	0.137	1.387		Le et al. [40]	0.187	1.34 ± 0.030	± 0.43
Goldstein (exp.) [3]	0.140			Linnick and Fasel [40]	0.197	1.34 ± 0.044	±0.69
Friehe (exp.) [55]	0.135			Frank et al. [24]	0.194	1.31	± 0.65
Mittal and Raghuvanshi [27]	0.142	1.489 ± 0.002	± 0.144	Berthelsen and Faltinsen [40]	0.200	1.37 ± 0.046	± 0.70
Present study	0.140	1.464 ± 0.003	±0.151	Present study	0.210	1.35 ±0.053	±0.53

vorticity contours are depicted in Fig. 14(a)–(c). The staggered nature of the Kármán shedding is clear from these plots. The crests and troughs of the sinuous waves in the streamlines reflect the alternatively positive and negative vorticities of the eddies. Apart from Figs. 13 and 14, the periodic nature of the flow is apparent from Fig. 15 where we have depicted the time evolution of the drag and lift coefficients for this Reynolds number. In Fig. 16, we compare the radial velocity values obtained by our computations at earlier stages along the axis of flow with those of the experimental results of Bouard et al. [31]. Note that $u^* = \dfrac{u}{U_\infty}$ and $x^* = \dfrac{x}{D}$ here. Our results match excellently with the experimental ones. In Fig. 17, vorticity distributions along the solid surface are shown for the same interval of time.

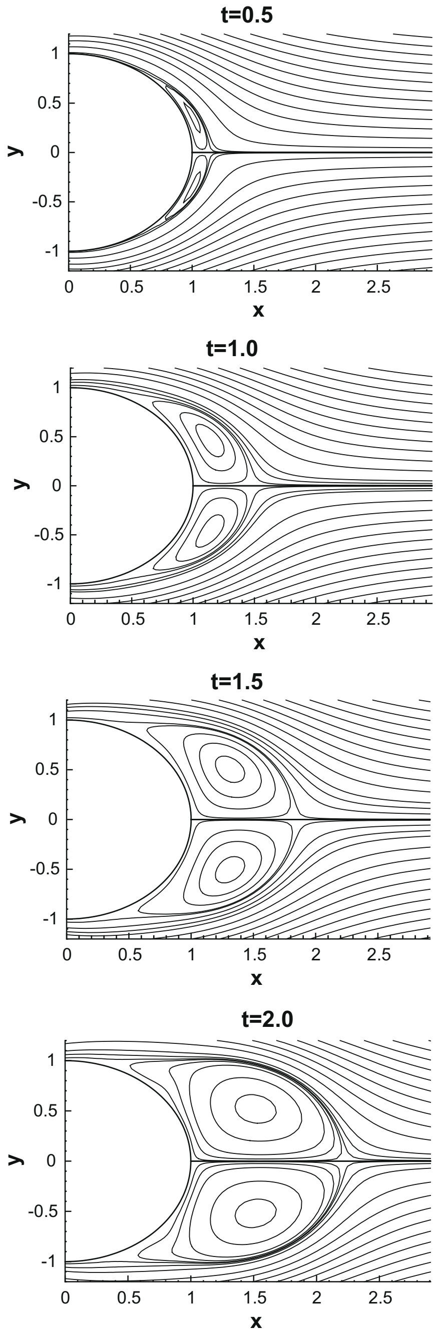

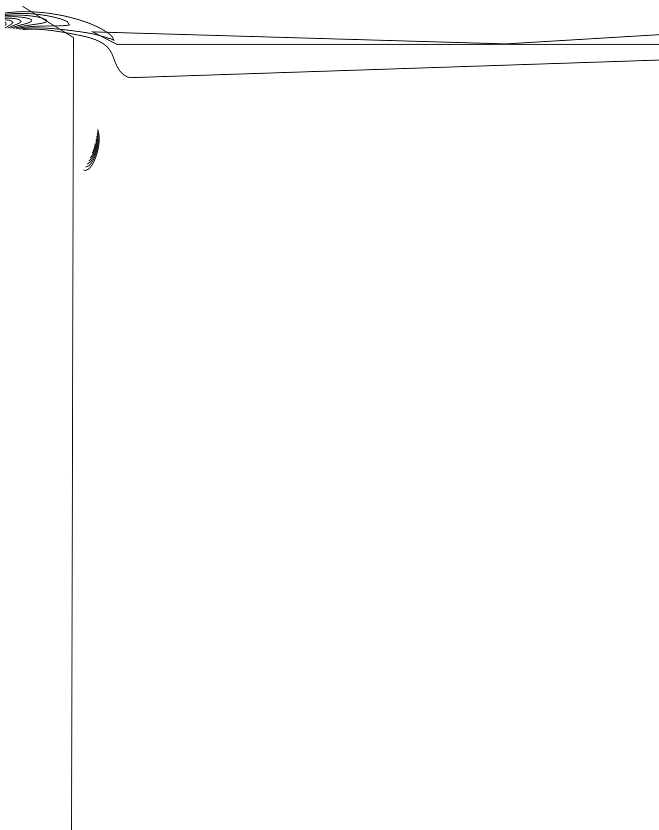

We also calculate the Strouhal St number for $Re = 60$ and 200, which characterizes the vortex shedding process and is estimated from the periodic variation of the lift coefficient. It is defined as $St = \frac{nD}{U_\infty}$ [32], where n is the dominant frequency of the lift variations, which we compute by a spectral analysis of a time sample of the lift coefficients. The power density spectra of this analysis is shown in Fig. 18(a). Fig. 18(b) displays the phase-plane of $u - v$ velocity at the monitoring point $(1.260, -0.067)$ for the same time sample; it clearly establishes the periodic nature of the flow for these two Reynolds numbers. In Table 4, we compare our computed Strouhal numbers, drag and lift coefficients for these two Re with established experimental and numerical results; for both Re, we obtain very close comparisons.

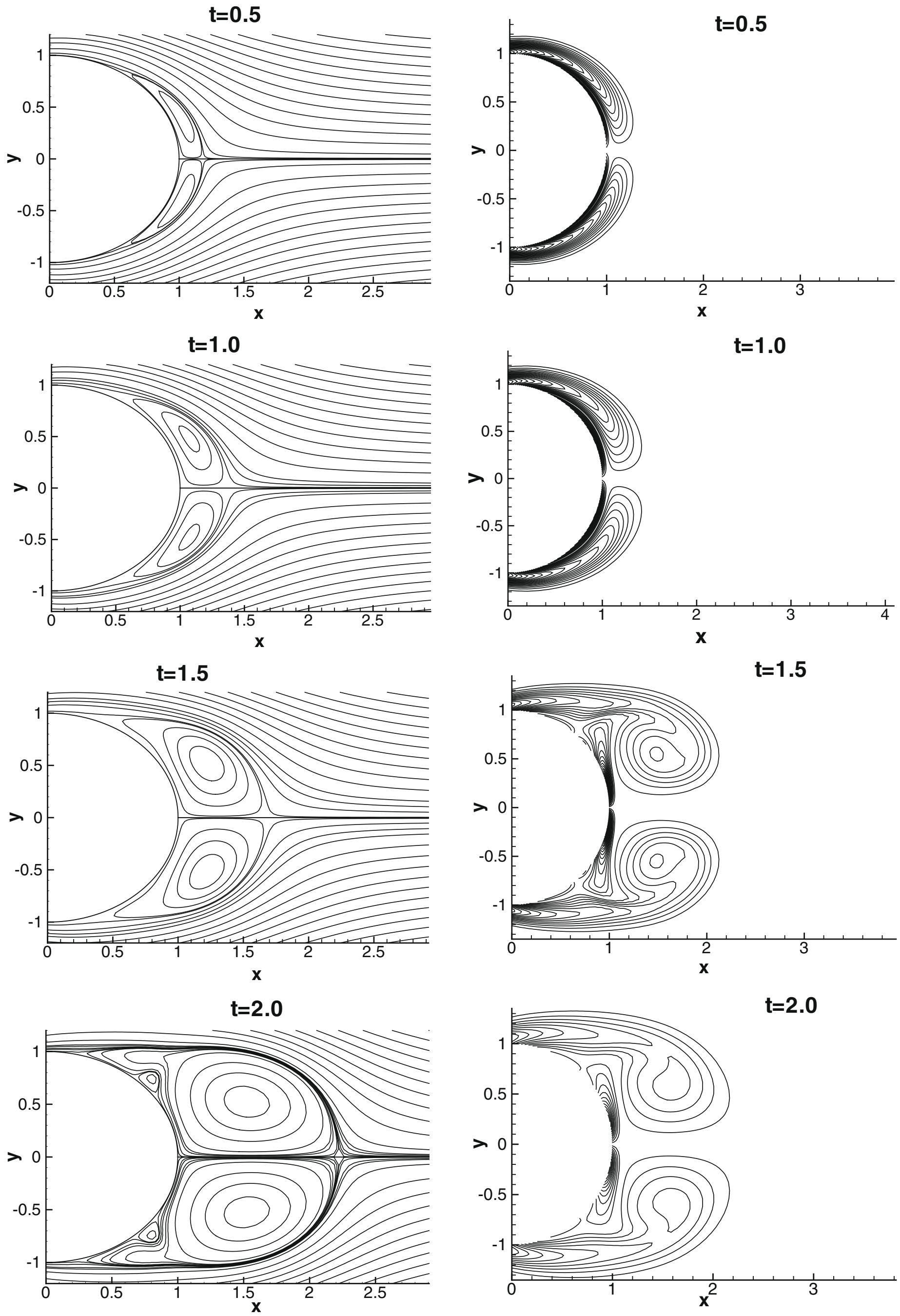

Fig. 20. Streamlines (left) and vortcity contours (right) for $Re = 550$ at different instants of time.

5.3. Flows for 300 and 550

For these two Reynolds numbers, the flow eventually becomes three-dimensional. For computational purpose, we have used a 181 × 181 grid for both *Re* values and R_∞ is taken as around 35 times of the cylinder radius for $Re = 300$, and 20 times of cylinder radius for $Re = 550$. We present the flow patterns for $Re = 300$ and $Re = 550$ at different instances of the early

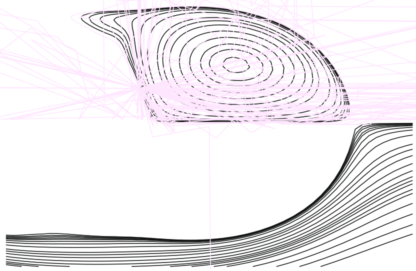

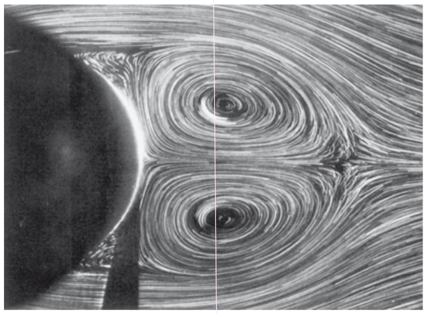

f

ly.

point

in the

00), this

Fig. 26. Far field ϵ 1.00: (a) $R_\infty = 5$ (top), (b) $R_\infty = 10$ (bottom).

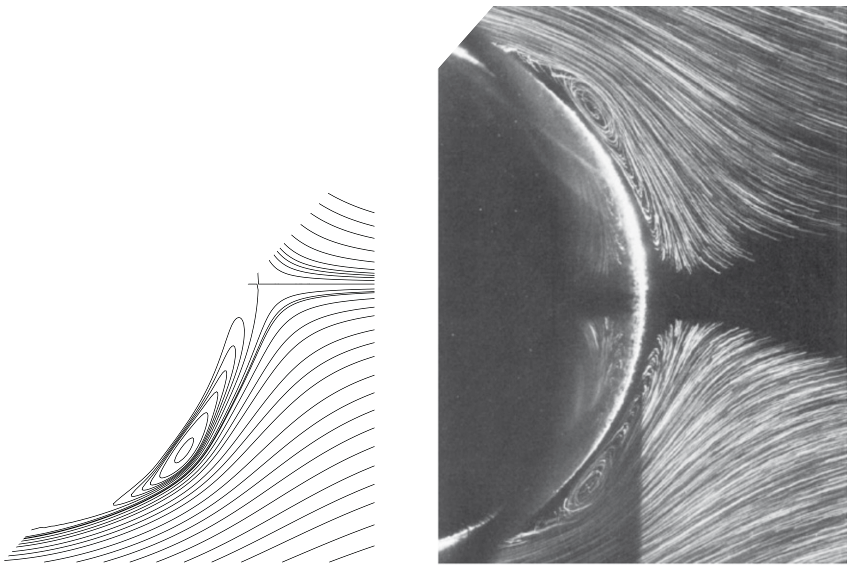

5.4. Flows for Re = 1000, 3000, 5000 and 9500

Flow around a cylinder at these Reynolds numbers eventually becomes three-dimensional and turbulent, and we do not intend to cover that regime. We only want to focus on the early stage of the flow development in which the two-dimensional laminar assumption has been justified by experiments. Another important feature of this flow range is that, the flow exhibits the so called α and β phenomena [31].

Experimental results [31] suggest that the α-phenomenon is distinctly visible in the range of Reynolds numbers $800 < Re < 5000$. As such, we start with $Re = 1000$ to present our numerical results depicting this phenomenon. Fig. 23(a) shows that at $t = 1.25$, the secondary vortex is yet to appear. Its appearance can be seen at $t = 1.75$ (Fig. 23(b)). When the primary vortex is still stable, the secondary vortex grows enough in size for its exterior boundary to touch the boundary of the main recirculating zone (Fig. 23(c) and (d)). Thus the main eddy is split into two parts and the region in the wake next to the separation point gets isolated and another secondary eddy is formed. These two secondary

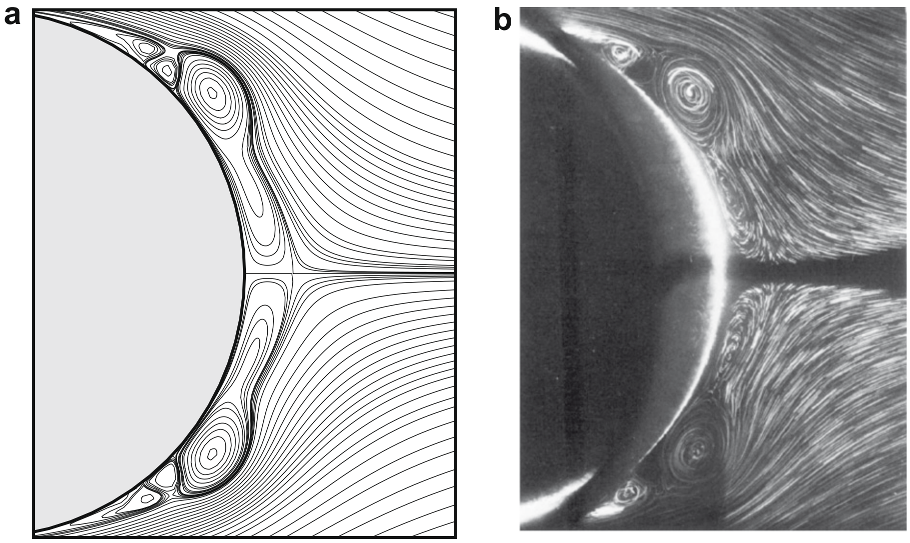

Fig. 28. The motion past a circular cylinder, streamlines for $Re = 9500$ at time $t = 1.00$: (a) Numerical (left), (b) Experimental (right [31]).

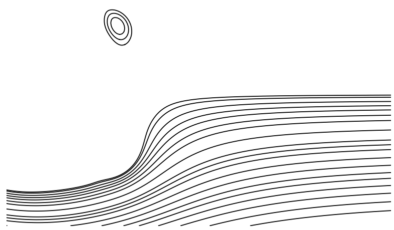

eddies thus formed are equivalent in strength and size and constitute a pair of secondary eddies (Fig. 23(e) and (f)). This is what is known as the α-phenomenon. The corresponding vorticity patterns for this time period are shown in Fig. 24(a)–(f) which are very close to the ones presented in [36,38,39,44]. The α-phenomenon for $Re = 3000$ can be seen in Fig. 25 where we present the simulation of the streamlines captured by our scheme at $t = 2.5$ side by side with the experimental results of

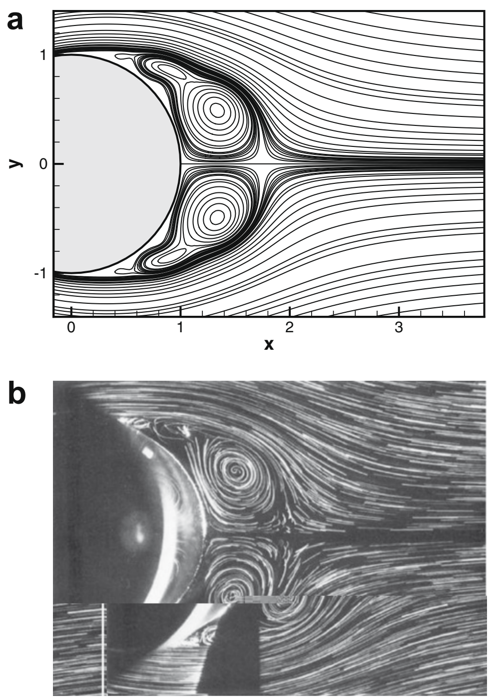

Fig. 30. The motion past a circular cylinder, streamlines for $Re = 5000$ at time $t = 1.50$: (a) Numerical (top), (b) Experimental (bottom [31]).

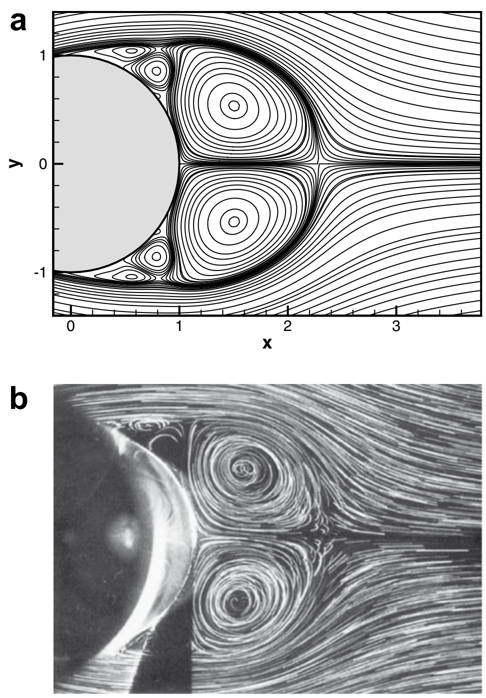

Fig. 31. The motion past a circular cylinder, streamlines for $Re = 5000$ at time $t = 2.00$: (a) Numerical (top), (b) Experimental (bottom [31]).

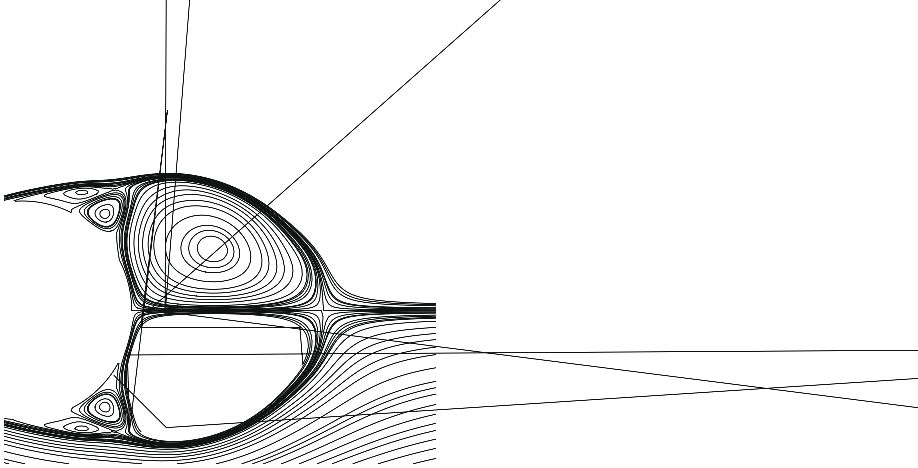

reference [31]. Again the experimental and numerical results are extremely close, thus demonstrating the robustness of our proposed scheme.

In Table 5, we present comprehensive data of the parameter values used for the Reynolds numbers considered for computation in the early stages of the flow. Here γ represents the under-relaxation parameter and N_{in} is the upper limit of the number of inner iterations required for the residual to fall below the tolerance limit as described in Section 4. As can be seen from the table, computational complexity increases with higher Reynolds numbers.

In Table 6, the effect of the grid size and the far field boundary conditions are presented for $Re = 9500$ at time $t = 1$. Fig. 26 compares the streamlines for $R_\infty = 5$ and $R_\infty = 10$ at the same instant on a grid of size 401×241. The table and the figures suggest that the influence of grid size and the domain of computation on the flow structure induces a slight variation. The percentage change in both L and θ_s were 0.8 as R_∞ was increased from 5 to 10.

Figs. 27 and 28 show the comparison of the experimental [31] and our computed results for the streamline patterns at time $t = 0.75$ and $t = 1.00$, respectively. In both the cases the match is very close. These two figures represent the so called β-phenomenon: at the very early stage of the flow (at around $t = 0.5$ [31]), a very thin recirculating wake (fitting exactly the cylinder shape) is formed; but soon afterwards at $t = 0.75$ (Fig. 27), the core of this recirculating zone rotates in one piece, much faster compared to the other part of the separated zone, forming a vortex which increases in size and strength with time. At time $t = 1.00$ (Fig. 28), this vortex separates the initial wake into two parts. The one situated near the point of separation S (as had been detailed in Fig. 5) is occupied by a pair of secondary vortices whose nature is similar to those that had been described for $Re = 1000$ and 3000, but differing in details. Interestingly, while only the β-phenomenon is observed for $Re = 9500$ at the very initial stage of the flow, for $Re = 5000$, both α and β phenomena are observed one after another [31,42,43]. Figs. 29 and 30 which compare the streamlines computed by the present scheme and the experimental results of [31] at time $t = 1.00$ and $t = 1.50$, respectively for $Re = 5000$ represent the β phenomenon. Likewise Figs. 31 and 32, depicting the numerical and experimental streamlines at $t = 2.00$ and $t = 2.50$, respectively represent the α-phenomenon. Some discrepancies between the experimental and numerical results for $Re = 5000$ in the early stage of the flow could be seen in some of the earlier reported results [25,41]. Our numerical results for this Reynolds number are probably closest to the experimental ones in terms of the size and shape of the vortices and wake lengths in comparison to other computations.

6. Conclusion

Differential equation based HOC schemes on geometries beyond rectangular, particularly on polar coordinates have so far been developed with the help of grid transformation only. In this paper, we develop an implicit, temporally second order accurate and spatially at least third order accurate scheme for the N–S equations in the $\psi - \omega$ form on nonuniform polar grids without transformation. We specifically fine-tune the scheme for simulating flows in the classical problem of unsteady incompressible viscous flow past an impulsively started cylinder. In the process, we have also developed compact higher order approximations for the Dirchlet boundary conditions for vorticity. We computed the flow for a wide range of Reynolds numbers ranging from 10 to 9500. The flow features which are typical of certain sub-ranges of the *Re* considered are discussed in details. We compare our results with established experimental and numerical results, and excellent comparison is obtained in all the cases, both qualitatively and quantitatively. The robustness of the scheme is highlighted when it captures the periodic nature of the flow for $Re = 60$ and 200 which is characterized by vortex shedding represented by the von Kármán street and also by the fact that it very accurately captures the so called secondary phenomena for moderate and α and β-phenomena for higher *Re*. The scheme also very efficiently and accurately captures the flow past a rotating cylinder, which will be discussed in our very next paper. The strength of our scheme is exemplified by the fact that flow simulations from our computations are much closer to the experimental visualization than other existing numerical simulations available in the literature, particularly for the higher Reynolds numbers.

Acknowledgment

The authors acknowledge M. Coutanceau and R. Bouard, the authors of reference [31], and also Cambridge University press for granting permission to reproduce pictures of experimental visualization in [31]. The authors are further grateful to the anonymous reviewers for their valuable comments which helped a lot in improving the quality of this paper.

Appendix A. Details of the finite difference operators

The expressions for the finite difference operators appearing in the various equations in Section 3 are as follows:

$$\delta_r\phi_{i,j} = \frac{\phi_{i+1,j} - \phi_{i-1,j}}{2\Delta r}$$

$$\delta_\theta\phi_{i,j} = \frac{\phi_{i,j+1} - \phi_{i,j-1}}{2\Delta\theta}$$

$$\delta_r^2\phi_{i,j} = \frac{1}{\Delta r}\left\{\frac{\phi_{i+1,j}}{r_f} - \left(\frac{1}{r_f} + \frac{1}{r_b}\right)\phi_{i,j} + \frac{\phi_{i-1,j}}{r_b}\right\}$$

$$\delta_\theta^2\phi_{i,j} = \frac{1}{\Delta\theta}\left\{\frac{\phi_{i,j+1}}{\theta_f} - \left(\frac{1}{\theta_f} + \frac{1}{\theta_b}\right)\phi_{i,j} + \frac{\phi_{i,j-1}}{\theta_b}\right\}$$

$$\delta_r^2\delta_\theta\phi_{i,j} = \frac{1}{2\Delta r\Delta\theta}\left\{\frac{1}{r_f}(\phi_{i+1,j+1} - \phi_{i+1,j-1}) - \left(\frac{1}{r_f} + \frac{1}{r_b}\right)(\phi_{i,j+1} - \phi_{i,j-1}) + \frac{1}{r_b}(\phi_{i-1,j+1} - \phi_{i-1,j-1})\right\}$$

$$\delta_r\delta_\theta^2\phi_{i,j} = \frac{1}{2\Delta r\Delta\theta}\left\{\frac{1}{\theta_f}(\phi_{i+1,j+1} - \phi_{i-1,j+1}) - \left(\frac{1}{\theta_f} + \frac{1}{\theta_b}\right)(\phi_{i+1,j} - \phi_{i-1,j}) + \frac{1}{\theta_b}(\phi_{i+1,j-1} - \phi_{i-1,j-1})\right\}$$

$$\begin{aligned}\delta_r^2\delta_\theta^2\phi_{i,j} = \frac{1}{\Delta r\Delta\theta}\Bigg\{&\frac{\phi_{i+1,j+1}}{r_f\theta_f} + \frac{\phi_{i-1,j+1}}{r_b\theta_f} - \left(\frac{1}{r_f\theta_f} + \frac{1}{r_b\theta_f}\right)\phi_{i,j+1} - \left(\frac{1}{r_f\theta_f} + \frac{1}{r_f\theta_b}\right)\phi_{i+1,j} \\ &+ \left(\frac{1}{r_f\theta_f} + \frac{1}{r_f\theta_b} + \frac{1}{r_b\theta_f} + \frac{1}{r_b\theta_b}\right)\phi_{i,j} - \left(\frac{1}{r_f\theta_b} + \frac{1}{r_b\theta_b}\right)\phi_{i,j-1} - \left(\frac{1}{r_b\theta_f} + \frac{1}{r_b\theta_b}\right)\phi_{i-1,j} \\ &+ \frac{\phi_{i+1,j-1}}{r_f\theta_b} + \frac{\phi_{i-1,j-1}}{r_b\theta_b}\Bigg\}\end{aligned}$$

$$\delta_r\delta_\theta\phi_{i,j} = \frac{1}{4\Delta r\Delta\theta}\{\phi_{i+1,j+1} - \phi_{i+1,j-1} - \phi_{i-1,j+1} + \phi_{i-1,j-1}\}.$$

Here $r_f = (r_{i+1} - r_i), r_b = (r_i - r_{i-1}), \theta_f = (\theta_{j+1} - \theta_j), \theta_b = (\theta_j - \theta_{j-1}), \Delta r = (r_f + r_b)/2$ and $\Delta\theta = (\theta_f + \theta_b)/2$ as defined in Section 3.

References

[1] C.T. Kelley, Iterative methods for linear and nonlinear equations, SIAM Publications, Philadelphia, 1995.
[2] Z. Kopal, Numerical Analysis, second ed., Chapman and Hall, London, UK, 1961.
[3] S. Goldstein, Modern developments in fluid dynamics, Clarendon Press, Oxford, 1938.
[4] J.C. Kalita, D.C. Dalal, A.K. Dass, A class of higher order compact schemes for the unsteady two-dimensional convection–diffusion equations with variable convection coefficients, Int. J. Numer. Methods Fluids 38 (2002) 1111–1131.
[5] J.C. Kalita, A.K. Dass, D.C. Dalal, A transformation-free HOC scheme for steady-state convection–diffusion on non-uniform grids, Int. J. Numer. Methods Fluids 44 (2004) 33–53.
[6] J.C. Kalita, A.K. Dass, N. Nidhi, An efficient transient Navier–Stokes solver on compact nonuniform space grids, J. Comp. Appl. Math. 214 (2008) 148–162.
[7] M.M. Gupta, R.P. Manohar, J.W. Stephenson, A single cell high order scheme for the convection–diffusion equation with variable coefficients, Int. J. Numer. Methods Fluids 4 (1984) 641–651.
[8] R.J. Mackinnon, R.W. Johnson, Differential equation based representation of truncation errors for accurate numerical solution, Int. J. Numer. Methods Fluids 13 (1991) 739–757.

[9] W.F. Spotz, G.F. Carey, High-order compact scheme for the steady stream-function vorticity equations, Int. J. Numer. Methods Eng. 38 (1995) 3497–3512.
[10] S.K. Lele, Compact finite difference schemes with spectral like resolution, J. Comput. Phys. 103 (1992) 16–42.
[11] M. Li, T. Tang, B. Fornberg, A compact fourth order finite difference scheme for the steady incompressible Navier–Stokes equations, Int. J. Numer. Methods Fluids 20 (1995) 1137–1151.
[12] Y. Adam, Highly accurate compact implicit methods and boundary conditions, J. Comput. Phys. 24 (1977) 10–22.
[13] R.S. Hirsh, Higher-order accurate difference solutions of fluid mechanics problems by a compact differencing technique, J. Comput. Phys. 19 (1975) 90–109.
[14] M.R. Visbal, D.V. Gaitonde, On the use of higher-order finite-difference schemes on curvilinear and deforming meshes, J. Comput. Phys. 181 (2002) 155–185.
[15] T.K. Sengupta, G. Ganeriwal, S. De, Analysis of central and upwind compact schemes, J. Comput. Phys. 192 (2) (2003) 677–694.
[16] S.E. Sherer, J.N. Scott, High order compact finite-difference methods on general overset grids, J. Comput. Phys. 210 (2005) 459–496.
[17] H. Blasius, Grenzschichten in Flussigkeiten mit kleiner Reibung, Z. Math. Phys. 56 (1908) 1–37.
[18] S. Goldstein, L. Rosenhead, Boundary layer growth, Proc. Cam. Phil. Soc. 32 (1936) 392–401.
[19] H. Schuh, Calculation of unsteady boundary layers in two-dimensional laminar flow, Z. Flugwiss. 1 (1953) 122–131.
[20] H. Wundt, Wachstum der laminaren Grenzschicht an schrag angestromten Zylindern bei Anfahrt aua der Ruhe, Ing.-Arch. Berlin 23 (1955) 212.
[21] E.J. Watson, Boundary layer growth, Proc. R. Soc. Lond. 231 (A) (1955) 104–116.
[22] C.Y. Wang, The flow past a circular cylinder which is started impulsively from rest, J. Math. Phys. 46 (1967) 195–202.
[23] W.M. Collins, S.C.R. Dennis, The initial flow past an impulsively started circular cylinder, Q. J. Mech. Appl. Math. 26 (1973) 53–75.
[24] R. Franke, W. Rodi, B. Schonung, Numerical calculation of laminar vortex-shedding flow past cylinders, J. Wind Eng. Ind. Aerodynam. 35 (1990) 237–257.
[25] T.K. Sengupta, R. Sengupta, Flow past an impulsively started circular cylinder at high Reynolds number, Comp. Mech. 14 (1994) 298–310.
[26] A. Dipankar, T.K. Sengupta, S.B. Talla, Suppression of vortex shedding behind a circular cylinder by another control cylinder at low Reynolds numbers, J. Fluid Mech. 573 (2007) 171–190.
[27] S. Mittal, A. Raghuvanshi, Control of vortex shedding behind circular cylinder for flows at low Reynolds numbers, Int. J. Numer. Methods Fluids 35 (2001) 421–447.
[28] S. Xu, Z.J. Wang, An immersed interface method for simulating the interaction of a fluid with moving boundaries, J. Comput. Phys. 216 (2006) 454–493.
[29] M. Coutanceau, R. Bouard, Experimental determination of the main features of the viscous flow in the wake of a circular cylinder in uniform translation. Part 1. Steady flow, J. Fluid Mech. 79 (1977) 231–256.
[30] M. Coutanceau, R. Bouard, Experimental determination of the main features of the viscous flow in the wake of a circular cylinder in uniform translation. Part 2. Unsteady flow, J. Fluid Mech. 79 (1977) 257–272.
[31] R. Bouard, M. Coutanceau, The early stage of development of the wake behind an impulsively started cylinder for $40 < Re < 10^4$, J. Fluid Mech. 101 (3) (1980) 583–607.
[32] D.J. Tritton, Experiments on the flow past a circular cylinder at low Reynolds numbers, J. Fluid Mech. 6 (1959) 547–567.
[33] S.C.R. Dennis, G.Z. Chang, Numerical solution for study flow past a circular cylinder at Reynolds numbers up to 100, J. Fluid Mech. 42 (1970) 471–489.
[34] B. Fornberg, A numerical study of steady viscous flow past a circular cylinder, J. Fluid Mech. 98 (1980) 819–855.
[35] B. Fornberg, Steady viscous flow past a circular cylinder up to Reynolds number 600, J. Comput. Phys. 61 (1985) 297–320.
[36] C.R. Anderson, M.B. Reider, A high order explicit method for the computation of flow about a circular cylinder, J. Comput. Phys. 125 (1996) 207–224.
[37] X. He, G. Doolen, Lattice Boltzmann method on curvilinear coordinates system: flow around a circular cylinder, J. Comput. Phys. 134 (1997) 306–315.
[38] L. Qian, M. Vezza, A vorticity-based method for incompressible unsteady viscous flows, J. Comput. Phys. 172 (2001) 515–542.
[39] R.K. Shukla, M. Tatineni, X. Zhong, Very high order compact finite difference schemes on non-uniform grids for incompressible Navier–Stokes equations, J. Comput. Phys. 224 (2007) 1064–1094.
[40] P.A. Berthelsen, O.M. Faltinsen, A local directional ghost cell approach for incompressible viscous flow problems with irregular boundaries, J. Comput. Phys. 227 (2008) 4354–4397.
[41] Y.V.S.S. Sanyasiraju, V. Manjula, Flow past an impulsively started circular cylinder using a higher-order semicompact scheme, Phys. Rev. E 72 (016709) (2005) 1–10.
[42] T.P. Loc, Numerical analysis of unsteady secondary vortices generated by an impulsively started circular cylinder, J. Fluid Mech. 100 (1980) 111–128.
[43] T.P. Loc, R. Bouard, Numerical solution of the early stage of the unsteady viscous flow around a circular cylinder: a comparison with experimental visualization and measurements, J. Fluid Mech. 160 (1985) 93–117.
[44] P. Koumoutsakos, A. Leonard, High-resolution simulations of the flow around an impulsively started cylinder using vortex methods, J. Fluid Mech. 296 (1995) 1–38.
[45] W.F. Spotz, G.F. Carey, Formulation and experiments with high-order compact schemes for nonuniform grids, Int. J. Numer. Methods Heat Fluid Flow 8 (3) (1998) 288–303.
[46] J. Zhang, L. Ge, M.M. Gupta, Fourth order compact difference scheme for 3D convection–diffusion equation with boundary layers on nonuniform grids, Nural Parallel Sci. Comput. 8 (2000) 373–392.
[47] S.K. Pandit, J.C. Kalita, D.C. Dalal, A transient higher order compact scheme for incompressible viscous flows on geometries beyond rectangular, J. Comput. Phys. 225 (2007) 1100–1124.
[48] M.C. Lai, A simple compact fourth-order Poisson solver on polar geometry, J. Comput. Phys. 182 (2002) 337–345.
[49] M.M. Gupta, A fourth order Poisson solver, J. Comput. Phys. 55 (1984) 166–172.
[50] S.R.K. Iyengar, R. Manohar, High order difference methods for heat equation in polar cylindrical coordinates, J. Comput. Phys. 77 (1988) 425–438.
[51] M.K. Jain, R.K. Jain, M. Krishna, A fourth-order difference scheme for quasilinear Poisson equation in polar co-ordinates, Commun. Numer. Methods Eng. 10 (1994) 791–797.
[52] Y. Zhuang, X.H. Sun, A high order fast direct solver for singular Poisson equations, J. Comput. Phys. 171 (2001) 79–94.
[53] C.H.K. Williamson, Oblique and parallel modes of vortex shedding in the wake of a circular cylinder at low Reynolds numbers, J. Fluid Mech. 206 (1989) 579–627.
[54] C. Norberg, An experimental investigation of the flow around a circular cylinder: influence of aspect ratio, J. Fluid Mech. 258 (1994) 287–316.
[55] C.A. Friehe, Vortex shedding from cylinders at low Reynolds numbers, J. Fluid Mech. 100 (1980) 237–241.